CHALMERS
UNIVERSITY OF TECHNOLOGY

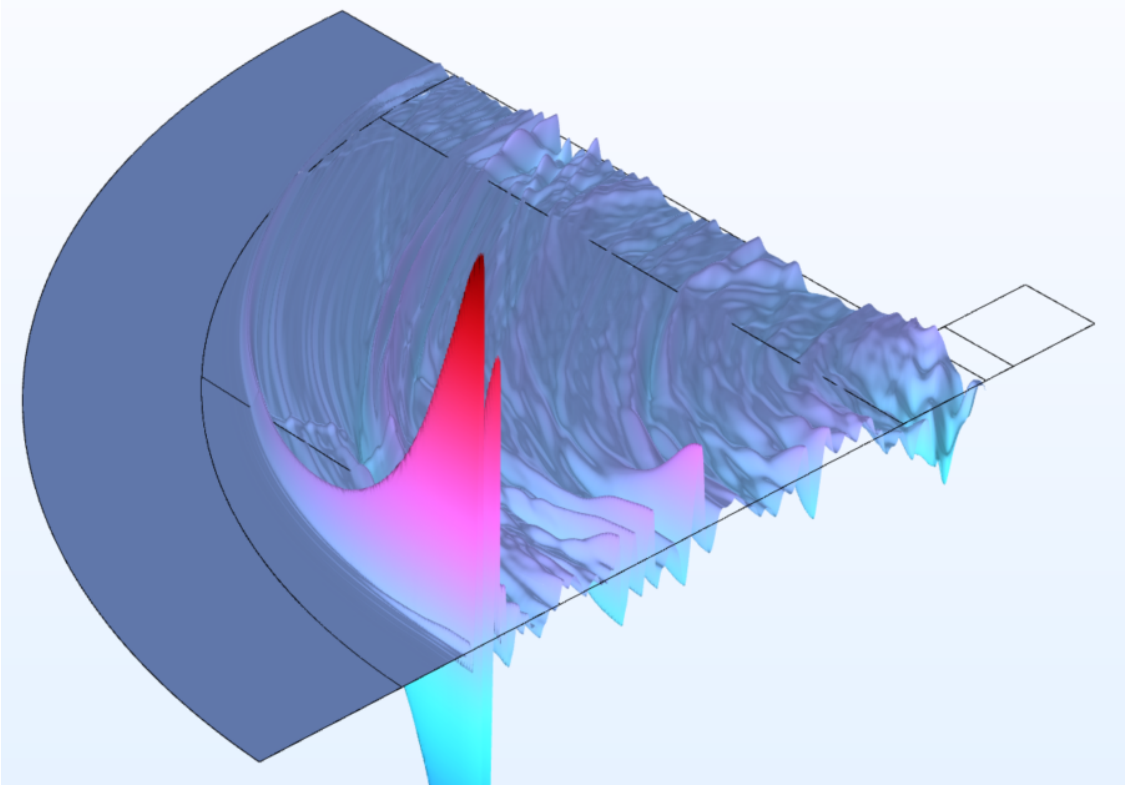

Computational Modeling of Cardiac Shockwave Therapy with Piezoelectric Transducers

Master's thesis in Complex Adaptive Systems

WILLEM DE WILDE

DEPARTMENT OF MECHANICS AND MARITIME SCIENCES

CHALMERS UNIVERSITY OF TECHNOLOGY
Gothenburg, Sweden 2024
www.chalmers.se

Master's Thesis in Complex Adaptive Systems

Computational Modeling of Cardiac Shockwave Therapy with Piezoelectric Transducers

WILLEM DE WILDE

CHALMERS
UNIVERSITY OF TECHNOLOGY

Department of Mechanics and Maritime Sciences
Division of Dynamics
Chalmers University of Technology
Gothenburg, Sweden 2024

Computational Modeling of Cardiac Shockwave Therapy with Piezoelectric Transducers
WILLEM DE WILDE

Supervisors: Henrik Staaf, RISE AB; Cristina Rusu, RISE AB
Examiner: Peter Folkow, Department of Mechanics and Maritime Sciences

Master's Thesis 2024
Department of Mechanics and Maritime Sciences
Chalmers University of Technology
SE-412 96 Gothenburg
Sweden
Telephone +46 31 772 1000

Cover: Acoustic pressure field generated by a piezoelectric shockwave transducer element, propagating through skin and fat tissues

Typeset in LaTeX
Gothenburg, Sweden 2024

Development of a Computational Model of Cardiac Shockwave Therapy
WILLEM DE WILDE
Department of Mechanics and Maritime Sciences
Division of Dynamics
Chalmers University of Technology

Abstract

Cardiac shockwave therapy (CSWT) has emerged as a promising treatment for ischemic heart disease, offering non-invasive rehabilitation options for patients suffering from myocardial infarction and refractory angina pectoris. This thesis focuses on developing a computational model to simulate the generation and propagation of acoustic waves associated with CSWT, emphasizing the role of piezoelectric transducers. Utilizing COMSOL Multiphysics, several models were implemented, including two-dimensional axisymmetric and one-dimensional plane wave propagation models, based on the nonlinear time explicit acoustic physics interface. The study also explores the design and simulation of piezoelectric transducers. Coupled simulations which model both piezoelectric transducers and acoustic propagation in biological tissue were implemented. Complex three-dimensional anatomical geometries were constructed, though not simulated. The numerical methods developed provide insights into the acoustic behavior of shockwaves within tissues, though experimental validation remains pending. This research contributes to the advancement of CSWT technology, potentially facilitating the development of a wearable device for self-administered CSWT.

Keywords: Cardiac Shockwave Therapy, COMSOL Multiphysics, Computational Acoustics, Nonlinear Acoustics, Piezoelectric Shockwave Transducer

Preface

This report presents the outcome of my master's thesis project carried out at the Department of Mechanics and Maritime Sciences at Chalmers University of Technology during the spring of 2024.

Acknowledgements

Writing the concluding words of this report, I get a strange feeling with the realization of eighteen years of studies coming to an end. From my first elementary school teacher Eivor to my supervisor Henrik, I have been grateful for having inspiring and competent teachers throughout these years.

Although I did this thesis project by myself, it has in many regards been a team effort. I have received great support from the people at the division of dynamics - that is Peter Folkow and Petri Piiroinen. They guided me to Håkan Wirdelius, who took the time to discuss the project and provided advice and expertise. The people working at RISE were always happy to bounce ideas and help with problems, both big and small. And a big 'thank you' goes to Vincent Uden who did his thesis project in the same office. Working back-to-back with Vincent, discussing, troubleshooting in the lab and cracking jokes made the time in the office much more rewarding!

Finally I want to express my gratitude to my family and my friends for putting up with me, both during the thesis project, and the years leading up to it. My parents, my sister and my brother-in-law have always encouraged me in all my adventures, while helping me keep my feet on the ground. My aunt Lilian also deserves a special 'thank you' - both for talking for hours about choosing a thesis project, and for being a role model by having an impressive career while being a selfless, caring and generous person.

There are more people that I want to thank, than can be listed here. But if you are reading this - there is a good chance that your name would be written here if only I had a few more pages available.

Thank you!

Willem de Wilde, Gothenburg, June 2024

List of Acronyms

Below is the list of acronyms that have been used throughout this thesis listed in alphabetical order:

CVD	Cardiovascular Disease
DGFEM	Discontinuous Galerkin Finite Element Methods
ECST	Extracorporeal Cardiac Shockwave Therapy
EFD	Energy Flux Density
HIFU	High Intensity Focused Ultrasound
IHD	Ischemic Heart Disease
LAPWE	Linear Acoustic Pressure Wave Equation
NATE	Nonlinear Pressure Acoustics, Time Explicit
PPP	Peak Positive Pressure
PVDF	Polyvinylidene fluoride
PZT	Lead zirconate titanate
SWL	Shockwave Lithotripsy
SWT	Shockwave Therapy

Nomenclature

Below is the nomenclature of parameters and variables that have been used throughout this thesis.

Generic material parameters

ρ	Material density
c_0	Speed of sound
ν	Poisson's ratio
Z	Acoustic impedance
δ	Acoustic diffusivity
α	Acoustic attenuation constant
β	Coefficient of nonlinearity

Piezoelectric material parameters

$\mathbf{D}$	Electric displacement vector
$\mathbf{T}$	Stress tensor
$\mathbf{E}$	Electric field vector
$\mathbf{S}$	Strain tensor
$\mathbf{d}$	Piezoelectric strain coefficient tensor
ϵ	Permittivity tensor
$\mathbf{s}^E$	Compliance tensor at constant electric field
$\mathbf{f}$	Body force per unit volume
$\mathbf{B}$	Magnetic flux density
ρ_f	Free charge density

Variables

λ	Wavelength
θ	Angle of incidence
p	Acoustic pressure
$\mathbf{u}$	Displacement vector
ω	Angular frequency
r, ϕ, z	Cylindrical spatial coordinates
t	Time

Contents

List of Figures

List of Tables

1
Introduction

1.1 Background

Cardiovascular disease (CVD) remains the most prevalent cause of death in the developed world at 23.7% in 2019 [1]. This is also the case in Sweden, where 30% of all death in 2022 were attributed to CVD, of which approximately one third were specified as due to ischemic heart disease (IHD) [2]. The life expectancy in Sweden has increased steadily during the last centuries, due to better care and more effective treatments among other factors [3]. However, it is important to consider a more nuanced picture than simply the life expectancy. Many people that get treatment for their cardiac condition still suffer from a degradation in their quality of life, which is more difficult to quantify. The Swedish Institute for Health Economics, presented in a report that CVDs cost the Swedish society over 60 billion SEK during 2019 - equal to over one percent of the Swedish gross domestic product the same year. The authors took both direct costs, such as the cost of care and treatment, and indirect costs such as lost productivity due to disabilities and premature deaths in consideration [4].

Cardiac shockwave therapy, or CSWT, is a form of treatment that shows promise in rehabilitation for patients who have suffered from a myocardial infarction, i.e. a heart attack, or are suffering from refractory angina pectoris, i.e. narrowing of the coronary vessels resulting in hypoxia in the myocardium during physical exertion, causing symptoms such as chest pain. The working princple is based on the transmission of high intensity acoustic pulses which exhibit shock formation, i.e. a very short pressure rise times, and their activation of biological processes associated with repair of tissue and symptom alleviation. A meta-analysis from 2020 by Yang et al., which included 26 clinical studies, concluded that CSWT provides beneficial effects to patients suffering from IHD [5].

The origins of the treatment lie in musculoskeletal shockwave therapy, which in turn was developed from shockwave lithotripsy (SWL), i.e. the disintegration of solids in the body, such as kidney- and renal stones, through the focused application of shockwaves [6]. In 1980, the first clinical use of the then novel SWL technology was seen in Germany. As SWL was widely adopted as a noninvasive treatment for renal stones, it was noticed that the shockwave therapy also promoted an increase in bone density, and stimulated healing in soft tissues. In the 1990s, much research was done on this phenomenon, and musculoskeletal SWT emerged as a treatment

for chronic pain conditions and conditions such as plantar fasciitis and tendinitis. SWT was observed to be effective for the promotion of cellular regeneration and angiogenesis, i.e. the generation of new vascular structures. These effects are further discussed in Section 2.1. The success of musculoskeletal SWT prompted researchers to investigate the efficacy of SWT in treating cardiac conditions. The first clinical application of CSWT was performed in 1999 on nine patients suffering from IHD [7]. This was the first study of many that concluded that CSWT is a safe technique, that improves cardiac function and perfusion, while decreasing symptoms of angina [6].

Since 1999, multiple studies and meta-analyses have been made on the efficacy of CSWT as a treatment for IHD. Although CSWT has been increasingly recognized for its potential to improve the health of sufferers from IHD, its adoption into mainstream medicine has been gradual. This can be attributed to several factors. The cost and accessibility of the specialized equipment required for CSWT can be a barrier to its widespread implementation. The technology and expertise needed to administer this therapy are as of yet only available in limited centers, primarily in research and specialized cardiac care facilities. However, many of these obstacles can be overcome by self-administering CSWT with a wearable device. This has the potential to reduce training requirements, cost, frequency of hospital visits, and bring other advantages. The development of such a device is the goal of the Swedish company CSW Therapeutics AB, which collaborates with Research Institutes of Sweden AB (RISE AB).

1.2 Purpose

RISE AB, is a research partner to the company CSW Therapeutics. The latter develops a wearable cardiac shockwave therapy device, intended for patients suffering from refractory angina and tissue damage following ischemic heart attacks. The purpose of this thesis project has been to provide both parties with simulation techniques and results that aid in product development.

1.3 Goals

This project has been conducted with several goals. These have included the following:

- Conducting a literature study
- Developing minimal numerical models of acoustic propagation in COMSOL Multiphysics
- Verifying the simulation results experimentally
- Modelling the interface between transducer and tissue
- Iteration and improvement of the simulation models to match experimental data
- Modelling of beam steering through phased-array-technology

These goals were to be extended with the development of an advanced anatomical physical tissue phantom, and the development of a full three-dimensional model, based on medical imaging.

1.4 Limitations / Demarcations

The scope of this thesis project was limited in its scope to employ currently available numerical methods. Only the physical aspects of the treatment were to be modeled, rather than the biological and physiological mechanisms.

2
Theory

2.1 Therapeutic effect of ECST

Although this report mainly focuses on the physical aspects of the generation of high intensity acoustic waves and their propagation in the tissues of the body, it is relevant to briefly explore their effects on the targeted tissue, as well as their potential side effects. The effects of different acoustic therapies are presented.

2.1.1 Effect of shockwaves on cardiac tissue

The working mechanisms of shockwave therapy are not yet fully understood, even if advancements have been made during the last years [8]. The effect of the therapy on biological tissue has been studied both *in vitro* and *in vivo*. Through mechanotransduction, i.e. biochemical reactions to mechanical stimulus, the applied shockwaves trigger a cascade of responses in the tissue on a cellular level. As presented in [6] and [9], observed effects on cardiac and vascular tissue include:

- Suppression of apoptosis, i.e. programmed cell death, in tissue adjacent to the necrotic, ischemic tissue
- Cellular proliferation, dependent on cell type. This is observed in both endothelial cells and cardiomyocytes
- Release of growth factor
- Increase of gene expression related to angiogenesis, i.e. generation of blood vessels
- Modulation of inflammation following myocardial ischemia

All these effects work to increase the rate of regeneration of cardiac function. It is worth noting that the repair mechanisms of tissue are activated even though no direct cellular damage is caused in the typical therapeutic range of CSWT.

In a recent study, Pölzl et al. presented guidelines for which acoustic energy flux densities (EFD) should be applied to ischemic cardiac tissue, to stimulate regeneration. This was based on both *in vitro* experiments where human umbilical vein endothelial cells were exposed to shockwaves of varying intensity, and *in vivo* experiments where ischemic limbs of mice were treated with SWT. The different parts of the study agreed that negative effects of SWT, such as cellular damage, are avoided with an EFD lower than 0.27 mJ/mm^2, and that the largest beneficial effects are reached at fluxes in the range of 0.07 - 0.15 mJ/mm^2 [9]. This is consistent with

values of EFD used in multiple studies on CSWT.

Although highly dependent on the waveform shape and pulse length, a linear fit on the data presented by Pölzl et al. indicates an approximately linear relationship between peak positive pressure (PPP) and EFD in cardiac shockwave therapy as:

$$\mathrm{PPP} \approx 2 \cdot 10^5 \mathrm{m}^{-1} \cdot \mathrm{EFD}. \tag{2.1}$$

This yields a PPP of approximately 40 MPa for a 0.27 $\mathrm{mJ/mm^2}$ shockwave. This value agrees with their measurements [9].

2.1.2 Possible side effects of CSWT

In their meta-analysis comprising 22 different studies with a total of 1189 treated patients, Burneikaitė et al. found no reported adverse effects resulting from CSWT. Patient discomfort during administration of the treatment has been reported in a few cases, but the lower intensity of the shockwaves imply that the risk of tissue damage is low, relative to the much higher EFD and pressures seen in SWL - usually with one order of magnitude higher PPP [10].

However, the acoustic pressure in the focal region can reach levels associated with tissue damage in gas filled structures, such as lungs, which are particularly vulnerable to tearing and mechanical damage. This is due to stress concentration and the incident and reflected waves being superposed. Research in the 1980s on canine and murine models indicated a limit on the acoustic pressure of pulsed ultrasound, before hemorrhages appeared in the lungs [11]. Acoustic pressures below 2 MPa applied to the lungs were deemed safe, while pressures of 10 MPa were observed to cause hemorrhages in some dogs. This underlines the need for precise aiming and focusing of the applied shockwaves.

Tears and necrosis have been observed in the tissues of the intestines, probably containing gas, after SWL for the treatment of renal stones [12]. SWL applied to gallstones located in the bile duct, near the diaphragm, risks transmission of shockwaves to the lungs if the direction of the shockwave is poorly controlled.

2.1.3 Effect of SWT on tissue

The effect of SWT in the context of musculoskeletal treatments has been documented and proven [13]. The biochemical responses are similar to those observed in CSWT, activating the repair mechanisms of the body through mechanotransduction. The technology has seen clinical use for about two decades. Success rates are high, and side effects are rare. SWT can also be utilized for sonoporation, a technique that uses acoustic waves to temporarily increase the permeability of cell membranes. the uptake of certain molecules in cells. This method shows promise in targeted drug delivery and gene therapy, providing a non-invasive means to improve the efficacy of treatments for various diseases.

2.1.4 Effect of High Intensity Ultrasound on tissue

High Intensity Focused Ultrasound (HIFU) is, similarly to SWT, a non-invasive acoustic therapeutic technique. It differs in that continuous focused ultrasound waves are employed to heat and destroy pathological tissue, such as tumors. HIFU is commonly used to treat prostate cancer, uterine fibroids, and other localized tumors. The primary mechanism of this treatment is the focused heating that follows the sonication of the tissues [14].

The thresholds for safe pressures in HIFU therapy are significantly higher than those in CSWT, often reaching PPPs of those seen in SWL. These high pressures are necessary to achieve the desired therapeutic effect, such as tumor ablation. However, they also increase the risk of adverse effects. The intense heat generated by HIFU can coagulate proteins and disrupt cellular membranes, leading to irreversible tissue damage. The rapid pressure changes can cause inertial cavitation, producing bubbles that collapse violently and generate shockwaves within the tissue. This can result in additional mechanical damage to both the targeted pathological tissue and the surrounding healthy tissues.

2.1.5 Effect of therapeutic ultrasound on tissue

Therapeutic ultrasound is a non-invasive modality used to enhance tissue healing and alleviate pain. Like HIFU, the technique utilize continuous high-frequency sound waves to create mechanical vibrations and thermal effects within targeted tissues. These trigger a range of physiological responses that aid in the healing process. However, as opposed to HIFU, the acoustic pressures are much lower, and the aim of the therapy is not to ablate or damage targeted tissues [14].

Therapeutic ultrasound primarily functions through two mechanisms: thermal and non-thermal effects. Thermal effects involve the conversion of ultrasound energy into heat, resulting in a slight local increase in tissue temperature and blood perfusion, thereby accelerating the healing process. Non-thermal effects, which occur even in the absence of significant temperature changes, include cavitation and acoustic streaming. Cavitation refers to the formation and oscillation of microscopic gas bubbles within the tissues. Note that this is not the same process as inertial cavitation, in which these bubbles collapse violently, damaging tissue. Rather, these bubbles can enhance cellular activities and increase membrane permeability, promoting cellular repair processes [15]. This technology was researched intensely around the 1980's, but has never seen widespread adoption. Although similar in its effects to SWT, its applications in cardiac medicine remain limited and mostly unexplored.

2.2 Characterization of acoustic waves

Acoustic waves can be classified into linear waves, shockwaves, and waves that exhibit properties in between these two extremes. Linear waves, governed by linear wave equations, maintain their shape and amplitude as they propagate. In con-

trast, shockwaves are highly nonlinear, characterized by abrupt changes in pressure and density, often resulting from high-energy events or nonlinear distortion. Waves that fall between these categories exhibit moderate nonlinearity where effects such as harmonic generation and wave distortion occur but are not as pronounced as in shockwaves [14].

As previously mentioned, it is difficult to compare the intensities of the applied acoustic waves in different studies. Many early medical studies specify the intensity of the shockwaves in terms of settings of the used apparatus. A common unit here is the voltage applied to the spark gap in electro-hydraulic shockwave transducers. In studies concerning SWL and SWT, the intensity is specified as the EFD, defined in Equation 2.2 as a factor times the time integral of the pressure squared integrated over a shockwave pulse. EFD is typically measured in mJ/mm^2. This parameter quantifies the amount of energy transmitted through the medium per unit area per shockwave. It provides a standardized measure for comparing the intensity of shockwaves across different devices and treatment protocols.

$$\mathrm{EFD} = \frac{1}{\rho c_0} \int_{t_0}^{t_1} p(t)^2 dt \tag{2.2}$$

However, variations in the focal zone, pulse frequency, and total number of shockwaves administered further complicate direct comparisons. For instance, studies on focused acoustic therapies often report EFD at the focal point, which can differ significantly from radial shockwave therapies that distribute energy more diffusely. The most commonly reported parameters include PPP, EFD, and pulse frequency, which offer summative or maximal values of the pressure-time waveform but do not detail its shape. A a consequence, observed biological effects in vitro have only been correlated with this limited set of physical parameters, lacking insights into the actual waveform dynamics and potential physical mechanisms. This illustrates the difficulty of comparing the applied acoustic waves in different studies [16].

In this context, Equation 2.1 provides some guidance in the comparison of numerical results and previous studies. This in combination with the evaluation of Equation 2.2 increases the confidence when evaluating the simulated performance of a CSWT transducer. However, it seems that further research is needed on the mechanisms and activation thresholds of mechanotransduction.

2.3 Shockwave transducers

Medical shockwave therapy employs various types of transducers to generate and deliver acoustic waves for therapeutic purposes. These transducers differ in their mechanisms and applications, each suited to specific needs. The primary types of shockwave transducers include electro-hydraulic, focused piezoelectric, electromagnetic [13] and radial transducers, though with some caveats for the latter [17]. It is worth noting that the electro-hydraulic type of transducer is the only ”true” shockwave transducer, which generates a shockwave directly, rather than the other listed technologies, which generate conventional acoustic pulses, with far longer pressure

rise times. These pulses form shock fronts during their propagation through nonlinear media, as described further in Sections 2.5.2 and 2.5.3.

2.3.1 Electro-Hydraulic Transducers

Electro-hydraulic transducers generate shockwaves using a high-voltage electrical discharge between two electrodes submerged in water. This discharge vaporizes the water, creating a rapidly expanding gas bubble that generates a shockwave. The shockwave is then focused by an ellipsoid reflector onto the target tissue. Electro-hydraulic transducers are known for producing high-intensity shockwaves with precise focal points, making them suitable for treatments such as lithotripsy, where high-energy shockwaves are required to break up renal stones. These transducers typically have a fixed focal point, although some advances have been made in achieving adjustable pressure field distribution and focal steering capability [18].

2.3.2 Focused Piezoelectric Transducers

Focused piezoelectric transducers utilize the piezoelectric effect, where materials such as certain ceramics generate mechanical stress and displacement in response to an electric field, and vice versa. These transducers are commonly composed of an array of piezoelectric elements arranged on a spherical surface. When an electrical pulse is applied, the elements expand, generating an acoustic wave. With sufficient amplitude and propagation distance, a shock front can form. These waves converge at a focal point, delivering concentrated energy to the target tissue. Focused piezoelectric transducers are favored for their precision and control, often used in applications requiring targeted therapeutic effects. These characteristics also make the technology suitable for CSWT, even if their power delivery is limited. Piezoelectric transducers are explored further in Section 2.4.

2.3.3 Electromagnetic Transducers

Electromagnetic transducers generate shockwaves by using a coil and a metallic membrane. When an electric current passes through the coil, it creates a magnetic field that rapidly propels the membrane. This movement generates an acoustic wave that is focused by an acoustic lens or reflector. Similarly to the piezoelectric variant, electromagnetic transducers produce consistent and controlled shockwaves with easily adjustable energy levels. The majority of CSWT transducers used in clinical studies have been of this type [10].

2.3.4 Radial Shockwave Transducers

Radial shockwave transducers produce pressure waves that radiate outward from the applicator's surface. The transducer has a relatively uniform radiation pattern. Unlike focused shockwaves, radial shockwaves have a more diffuse energy distribution. The radial transducers typically use a ballistic mechanism, where a projectile is accelerated towards an applicator by either pneumatic or electromagnetic forces.

Upon impact, the energy is transferred radially into the tissue. Radial transducers are commonly used for treating superficial musculoskeletal conditions, such as tendinitis. The penetration depth is limited compared to focused shockwave technologies, but the treatment is easily applied to a larger area. It must also be noted that this type of transducer, although clinically effective, does not form shockwaves in the physical sense, but rather high amplitude acoustic waves, with far longer pressure rise times than shock waves [17].

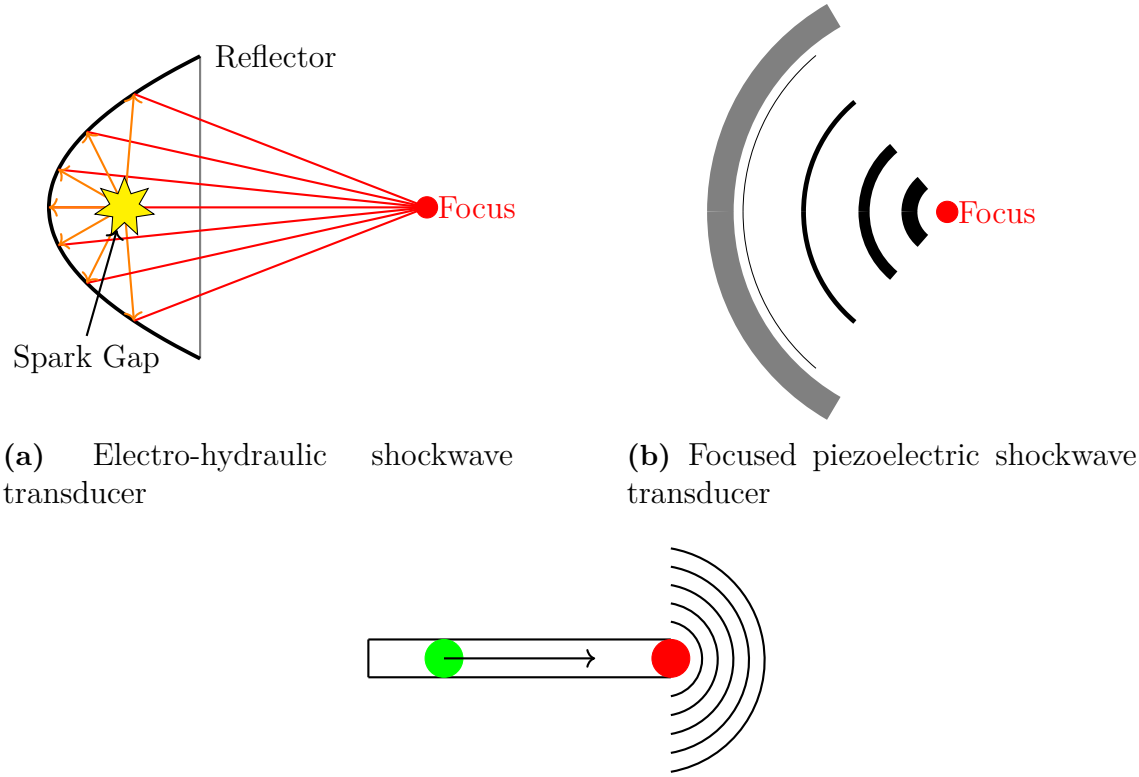

(a) Electro-hydraulic shockwave transducer

(b) Focused piezoelectric shockwave transducer

(c) Ballistic type radial shockwave transducer

Figure 2.1: Schematics of different types of shockwave transducers.

2.4 Piezoelectric transducers

Piezoelectric materials are widely used in various applications, including sensors, actuators, and energy harvesting devices, due to their ability to directly convert mechanical energy into electrical signals. The product developed by CSW Therapeutics is based on piezoelectric transducers. For the experimental part of this project, a piezoelectric transducer element was designed.

2.4.1 Piezoelectricity

Piezoelectric materials exhibit the unique property of converting mechanical energy into electrical energy and vice versa. This phenomenon is governed by the coupled

electromechanical behavior described by the piezoelectric equations. The fundamental principles of piezoelectricity are conveyed through the constitutive equations, which relate mechanical stresses and strains to electrical fields and displacements [19].

The linear constitutive equations for piezoelectric materials can be expressed as:

$$\begin{cases} \mathbf{D} = \mathbf{d} \cdot \mathbf{T} + \varepsilon \cdot \mathbf{E}, \\ \mathbf{S} = \mathbf{s}^E \cdot \mathbf{T} + \mathbf{d}^T \cdot \mathbf{E}, \end{cases} \tag{2.3}$$

where the variables represent different physical quantities as described in Table 2.1 below. These equations describe the direct piezoelectric effect, i.e. how an applied

Variable	**Description**	**Dimension (rank)**	**Unit**
$\mathbf{D}$	Electric displacement vector	3-dim. vector (rank 1)	C/m^2
$\mathbf{T}$	Stress tensor	3x3 tensor (rank 2)	Pa
$\mathbf{E}$	Electric field vector	3-dim. vector (rank 1)	V/m
$\mathbf{S}$	Strain tensor	3x3 tensor (rank 2)	1 (or m/m)
$\mathbf{d}$	Piezoelectric strain coefficient tensor	3x6 tensor (rank 3)	C/N (or m/V)
ε	Permittivity tensor	3x3 tensor (rank 2)	F/m
$\mathbf{s}^E$	Compliance tensor at constant electric field	6x6 tensor (rank 4)	m^2/N
$\mathbf{F}_V$	Body force per unit volume	3-dim. vector (rank 1)	N/m^3
ρ	Material density	Scalar	kg/m^3
$\mathbf{u}$	Displacement vector	3-dim. vector (rank 1)	m
$\mathbf{v}$	Local velocity vector	3-dim. vector (rank 1)	m
ρ_f	Free charge density	Scalar	C/m^3
$\mathbf{D}_r$	Remanent electric displacement	3-dim. vector (rank 1)	C/m^2
$\mathbf{P}(\mathbf{E})$	Nonlinear polarizing field dep. on $\mathbf{E}$)	3-dim. vector (rank 1)	C/m^2

Table 2.1: Variables, their descriptions, dimensions, and units in piezoelectric materials

mechanical stress $\mathbf{T}$ generates an electric displacement $\mathbf{D}$. They also describe the inverse piezoelectric effect - how an applied electric field $\mathbf{E}$ induces a mechanical strain $\mathbf{S}$.

The dynamic behavior of piezoelectric materials is more complex and is influenced by the inherent coupling between electrical and mechanical states. The governing equations for the dynamics can be derived from the general principles of continuum mechanics and electrodynamics.

2.4.2 Coupled Field Equations

Combining the mechanical and electrical governing equations, we obtain the coupled field equations, Equations 2.4 - 2.8, that describe the behavior of piezoelectric materials under dynamic loading conditions. These equations take into account both mechanical deformations, inertial effects and electric field interactions, leading to a set of partial differential equations that must be solved simultaneously. The complexity of these equations often requires numerical methods for practical analysis and design of piezoelectric devices.

Assuming linear dependencies between stress and strain, and between stress and electrical displacement in the absence of an external electric field, the following equations are valid [20]:

$$\rho \frac{\partial \mathbf{v}}{\partial t} - \nabla \cdot \mathbf{T} = \mathbf{F}_V \tag{2.4}$$

$$\frac{\partial \boldsymbol{S}}{\partial t} - \frac{1}{2}\left[\nabla \mathbf{v} + (\nabla \mathbf{v})^T\right] = 0 \tag{2.5}$$

$$\nabla \cdot \mathbf{D} = \rho_f \tag{2.6}$$

$$\mathbf{S} = \mathbf{s}^E \cdot \mathbf{T} + \mathbf{d}^T \cdot \mathbf{E} \tag{2.7}$$

$$\mathbf{D} = \mathbf{D}_r + \varepsilon_0 \mathbf{E} + \mathbf{P}(\mathbf{E}) + \mathbf{ds}^E : \boldsymbol{S} \tag{2.8}$$

Here the colon operator denotes the double-dot tensor product.

2.4.3 Transducer design

As all experimental methods require the transmission of acoustic energy, and the available hardware for this was limited to simple ceramic piezoelectric disks, constructed in silver-metallized lead zirconate titanate (PZT), it was necessary to construct improved transducer units, based on these disks. This subsection provides the theoretical background for this.

2.4.3.1 Impedance matching

The acoustic impedance Z of high performance piezoelectric ceramics is around one order of magnitude larger than that of soft tissues.

$$Z = \rho \cdot c_0 \tag{2.9}$$

The reflected and transmitted pressures, p_r and p_t, given a wave with pressure p_i incident to a material discontinuity where the source and target material have acoustic impedances Z_1 and Z_2 respectively, are given by:

$$p_r = p_i \left(\frac{Z_2 - Z_1}{Z_2 + Z_1}\right), \tag{2.10}$$

$$p_t = p_i \left(\frac{2Z_2}{Z_2 + Z_1} \right). \tag{2.11}$$

Disregarding reflections, it follows that a wave transmitted through n boundaries has the pressure p_t:

$$p_t = p_i \prod_{i=1}^{n} \left(\frac{2Z_{i+1}}{Z_{i+1} + Z_i} \right). \tag{2.12}$$

Examining this equation, we conclude that the transmitted pressure is higher if a coupling medium with an intermediate acoustic impedance is used. It is also evident that liquid-gas interfaces reflect the absolute majority of the signal, as their acoustic impedances differ by about 4 orders of magnitude. Due to this, a coupling medium, e.g. a gel, is necessary to match the impedance between the transducer and the tissue. In order to increase the transmission further, the transducer often employs a coupling layer between the piezoelectric ceramic and coupling medium. Designs with multiple coupling layers are not uncommon. The optimum intermediate impedance is given by:

$$Z_{opt} = \sqrt{Z_1 Z_2}. \tag{2.13}$$

The effective transmission can also be increased considerably by tuning the thickness of the coupling layer to odd multiples of one fourth of the wavelength λ, as reflections are minimized through destructive interference. Commonly seen thicknesses are either $\lambda/4$ or $3\lambda/4$.

2.4.3.2 Backing

The backing of piezoelectric elements is important to their performance in acoustic transducers. Common materials include epoxy with tungsten powder or similar high-density substances, providing both acoustic impedance matching and mechanical stability. The acoustic impedance of the backing layer is often set to be equal to that of the piezoelectric ceramic. This increases the transducer's bandwidth, as no standing waves form [21].

However, a higher transmitted amplitude can be achieved in some cases by employing an air-backed transducer. Constructive interference at the transmitting face of the element increases the transmitted power. The gain in amplitude is at the expense of a much narrower bandwidth, and longer ring-down times. In other words, an air-backed transducer gains some of the characteristics of an oscillator. This may be suitable for producing the harmonic fields required in HIFU and conventional ultrasound, but might not be desirable when aiming to transmit a single pressure pulse, containing multiple spectral components. Air-backed piezoelectric transducers are typically underdamped, with ring down times much longer than an oscillation period. This means that they exhibit a high Q factor, which is defined as the ratio of the transducer's center frequency to its bandwidth.

2.4.3.3 Electrical matching

Electrical impedance matching of the capacitance inherent to piezoelectric transducers affects energy transfer and impulse response. One common method for achieving

a balanced and more resonant electrical circuit is to use an inductance L in series with the transducer to compensate for its capacitive reactance. The required value of L as to balance the circuit can be calculated using the formula:

$$L = \frac{1}{\omega^2 C} \tag{2.14}$$

where ω is the mechanically resonant angular frequency and C is the capacitance of the transducer. The RLC-circuit is a simple model, and more complex considerations, such as cable impedance can also be accounted for [22]. Tuning the inductance improves energy transmission efficiency, but decreases bandwidth as the system is optimized for its resonance frequency. Similarly to introducing backing, this may or may not be desirable, depending if the goal is to maximize harmonic oscillation and energy delivery, or to achieve a wide bandwidth.

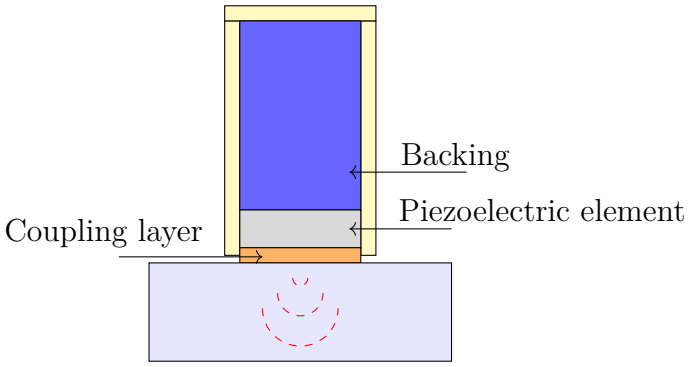

Figure 2.2: Schematic of typical piezoelectric transducer element

2.4.4 Focused piezoelectric shockwave transducers

To increase the acoustic pressure, the acoustic field generated by piezoelectric transducers can be focused into a small region, i.e. a focal spot, after which the field diverges. This can be accomplished through different methods. Single-element transducers, where a spherically shaped and polarized single element generates the pressure wave, will have a fixed focal point by design. Cylindrical geometries are also prevalent, focusing the field onto a line. An alternative to a single element transducers are transducer arrays, where smaller transducer elements are distributed on a surface, and their signals combined through constructive interference. A synchronized activation of these elements will also result in a fixed focal spot, if on a spherical surface [14].

However, in medical applications, it is often desirable to guide the focal point automatically, rather than repositioning the entire transducer. This is known as focal steering, and can be implemented by controlling each transducer element individually, controlling its delay and amplitude, i.e. by using a phased array. The region that can be targeted by a transducer array is known as its field of view, which influenced by the radiation pattern of the transducer elements, and the geometry of the array itself. These are used extensively in HIFU therapies. For applications in

SWT, propagation distance is needed for the cumulative nonlinear acoustic effects to result in shock formation. This distance is influenced by the local pressure gradient, i.e. field concentration, amplitude and pressure rise time [14].

2.5 Acoustic propagation

In this section, the different types of acoustic propagation mentioned in Section 2.2 are discussed further, and their governing equations listed.

2.5.1 Linear propagation

$$\frac{1}{c^2}\frac{\partial^2 p_t}{\partial t^2} - \nabla^2 p_t = 0 \tag{2.15}$$

This is equivalent to the equation solved by COMSOL Multiphysics, *Pressure Acoustics, Transient*, with the *Linear elastic* fluid model. The solved equation is specified as:

$$\frac{1}{\rho c^2}\frac{\partial^2 p_t}{\partial t^2} + \nabla \cdot \left(-\frac{1}{\rho}(\nabla p_t - \mathbf{q}_d)\right) = Q_m, \tag{2.16}$$

where $\mathbf{q}_d$ and Q_m denote the dipole- and monopole domain pressure sources respectively [23]. These terms are usually equal to zero if no external driving forces are present. In this case, inspection and the identity $\nabla^2\phi = \nabla \cdot (\nabla\phi)$ yields equality to the previous equation.

The linear acoustic pressure wave equation, or LAPWE model is easy to implement with popular PDE solving algorithms. As a scalar equation, its implementation is straightforward [14]. It accounts for classic wave propagation phenomena, including reflection, refraction, and scattering. However, it does not account for energy absorption. This can be adressed by modifying the LAPWE PDE. An attenuated linear model can be formed with the addition of a damping term, proportial to the time derivative of the Laplacian of the scalar pressure field:

$$\frac{1}{\rho c^2}\frac{\partial^2 p_t}{\partial t^2} + \nabla \cdot \left(-\frac{1}{\rho}(\nabla p_t - \mathbf{q}_d) + \frac{\delta}{\rho c^2}\frac{\partial \nabla p_t}{\partial t}\right) = Q_m \tag{2.17}$$

As the time derivative of the pressure increases proportionally with the frequency of the signal, it is clear that the damping term grows linearly with frequency. This is not an ideal model, as many materials exhibit a nonlinear dependency between the attenuation coefficient α and signal frequency, in the form of a power law:

$$\alpha(\omega) = \alpha_0 \omega^\eta \tag{2.18}$$

Many tissues have a non-unity value of η, invalidating the linear relationship in the model. Most soft tissues have a rather small value of η between 1 and 2. As nonlinear effects become dominant, harmonics of many times the fundamental frequency can arise. These harmonics are subject to a larger discrepancy in the attenuating

coefficient, as $\alpha \propto N^{\eta}$. However, the linear approximation of the exponential relationship is deemed acceptable for the case of muscular tissue where η has been experimentally estimated to be in the range 1 - 1.2. The attenuation of higher frequencies can be modeled with methods known as shock-capturing stabilization, discussed further in Subsection 2.5.3 [24].

2.5.2 Nonlinear propagation

The propagation of acoustic waves is often thought of as a simple phenomenon. If the governing equations are linear, such as in LAPWE, the transmitted signal is not distorted. The medium density and speed of sound is thought of constant for all pressures and frequencies. This approximation holds true for infinitesimally small acoustic signals. However, as amplitudes and pressure gradients increase, nonlinear effects become non-negligible. The propagation medium also has a large influence on the distortion of the waveform [25].

In essence, the pressure wave is distorted due to a nonlinear relationship between the acoustic pressure and the displacement of the medium. An example which is easy to visualize is a porous medium, such as a gel with bubbles dispersed in the material. These cavities will expand easily at negative pressures, i.e. tensile stresses. As the voids are compressed, the compressibility of the material decreases rapidly. This is the case in inflated lung tissue. However, materials and fluids in particular also exhibit this behaviour even if no gas voids are present. Due to these effects, the PPP tends to be less attenuated with propagation distance than the absolute negative pressure.

The extent of these characteristics is commonly described by the coefficient of nonlinearity B/A, where A and B denote the first and second terms in the Taylor expansion of the function relating the pressure of the propagation medium to its density. These terms are included in the coefficient β defined as:

$$\beta = 1 + \frac{B}{2A} \tag{2.19}$$

Naturally, there are more non-zero terms than the two first, but these are rarely used. This notation yields more compact expressions in the governing differential equations describing the wave propagation.

Non-linear acoustic propagation can be modeled by adding a second-order term to Equation 2.17. By assuming that the cumulative effects of non-linear propagation are greater than the local effects, which for example is the case if the propagation distance is much greater than the wavelength, one can derive the Westervelt Equation (2.20), which models the pressure - density relationship as a parabolic function. Disregarding the source terms $\mathbf{q}_d$ and Q_m, we obtain [23]:

$$\frac{1}{\rho c^2}\frac{\partial^2 p_t}{\partial t^2} + \nabla \cdot \left(-\frac{1}{\rho}\nabla p_t + \frac{\delta}{\rho c^2}\frac{\partial \nabla p_t}{\partial t} \right) = \frac{\beta \partial^2 p_t^2}{\rho^2 c^4 \partial t^2}. \tag{2.20}$$

The linear approximation is valid to acoustic pressures far lower than the expression:

$$| p | << \rho c^2, \tag{2.21}$$

However, nonlinear effects on the waveform are cumulative, meaning that the propagation distance also plays into the consideration if a linear model is a sufficient approximation. Naturally, the coefficient of nonlinearity also has a large influence, and which approximations to be made has to be assessed for each case. [23]

2.5.3 Shockwave formation and propagation

As previously mentioned, acoustic shockwaves can emerge through various processes. Detonation, as seen with electro-hydraulic shockwave transducers, or the activation of explosives, generates shockwaves directly. Additionally, shockwaves can form through the distortion of conventional acoustic waves. Shockwave formation from a sinusoidal wave begins with nonlinear propagation, where higher pressure portions of the wave travel faster than lower pressure portions. This velocity difference causes the wavefront to steepen as it propagates, compressing the waveform's leading edge. Over time and distance, this steepening effect accumulates, transforming the initially smooth sinusoidal wave into a sharp, discontinuous shockwave. However, the higher harmonics of the shockwave are, as discussed previously, attenuated faster than the lower harmonics and the fundamental frequency, leading to the gradual return to a smoother waveform, eventually approaching a signal with the pure fundamental frequency, albeit with much lower amplitude [26].

Modelling of shockwave propagation is computationally expensive, due to the high number of harmonics that are required to be resolved by the mesh. This problem can be partially solved by using q-Laplacian relaxation [23]. The term

$$-\kappa \left(1 - \left|\frac{\partial}{\partial t}\nabla p\right|^{q-1}\right) \tag{2.22}$$

is added as a factor to the damping term on the left hand side of the Westervelt Equation 2.20, resulting in the full PDE:

$$\frac{1}{\rho c^2}\frac{\partial^2 p_t}{\partial t^2} + \nabla \cdot \left(-\frac{1}{\rho}(\nabla p_t - \mathbf{q}_d) - \frac{\delta}{\rho c^2}\left[1 - \kappa\left(1 - \left|\frac{\partial \nabla p_t}{\partial t}\right|^{q-1}\right)\right]\frac{\partial \nabla p_t}{\partial t}\right) = Q_m. \tag{2.23}$$

In order to preserve numerical stability at solution discontinuities, Equation 2.20 is formulated in its conservative form, as a coupled PDE [23]:

$$\frac{1}{\rho c^2}\frac{\partial p_t}{\partial t} + \nabla \cdot \left[\left(1 + \frac{\beta p_t}{\rho c^2}\right)\mathbf{u}_t\right] = Q_m, \tag{2.24}$$

$$\rho \frac{\partial \mathbf{u}_t}{\partial t} + \nabla \cdot (p_t \mathbf{I}) = \mathbf{q}_d + \rho\delta\Delta\mathbf{u}_t, \tag{2.25}$$

where $\mathbf{u}_t$ is the local particle velocity vector. This equation is solved numerically by COMSOL multiphysics NATE interface, calculating the time evolution of the local velocity and the acoustic pressure, given initial- and boundary conditions.

2.5.4 Numerical solution of the PDEs

Discontinuous Galerkin Finite Element Methods (DGFEM) are a group of algorithms for solving the previously listed governing PDEs of acoustic wave propagation. DGFEM are employed in the NATE interface of COMSOL Multiphysics. It is favored due to its high accuracy and flexibility in handling complex geometries and boundary conditions, as well as its efficient parallel computations [23]. It is particularly effective in capturing sharp gradients and discontinuities in acoustic fields, such as in nonlinear acoustic modeling. DGFEM also constitutes a memory efficient method for solving these equations, which is increasingly important as the DoF increase. The DGFEM algorithms are complex and it is beyond the scope of this report to compile the equations. The use of a WENO (Weighted Essentially Nonoscillatory) limiter is recommended in COMSOL Multiphysics as to preserve numerical stability for simulation of highly nonlinear acoustic propagation, with the coupled PDEs.

2.5.5 Structure - acoustic coupling

The interface between two propagation media can be modeled as the continuity of normal velocity and pressure at the boundary. This will take the effects of reflection and transmission, and conservation of energy into account.

$$\mathbf{n} \cdot (\mathbf{v} - \mathbf{u}_t) = 0 \tag{2.26}$$

$$\mathbf{n} \cdot (\mathbf{T} + p\mathbf{I}) = 0 \tag{2.27}$$

Here, $\mathbf{n}$ is the normal vector to the coupling surface, $\mathbf{v}$ is the local velocity in the piezoelectric material and $\mathbf{u}_t$ that in the acoustic medium, p is the acoustic pressure, and $\mathbf{I}$ is the identity matrix, here specifying that the pressure is isotropic on the boundary. Note that the convention in continuum mechanics is to denote stress as $\mathbf{S}$ rather than $\mathbf{T}$. For the sake of unambiguity, the same notation is used here as in Section 2.4.

3
Methods

The goal of this project has been the development of the numerical methods. Hence, these methods are explored in detail. The outputs and predictions of these methods were to be verified through experimental measurements. These experiments were planned and designed, but were never performed due to practicalities, briefly explained in Subsection 3.8. Due to this, the project was given an almost purely computational focus.

3.1 Literature study

The literature study was conducted to establish understanding of existing knowledge and methodologies relevant to the simulation model development. This involved a review of scholarly articles, conference papers, and relevant textbooks. Keywords were selected based on the research objectives, focusing on terms such as ”cardiac shockwave therapy”, ”HIFU simulation”, ”shockwave simulation”, ”piezoelectric transducer modeling” and ”shockwave transducer”.

Major academic databases and search tools such as IEEE Xplore, Scopus, ScienceDirect, and Google Scholar, as well as the search functions of Chalmers Library were used to source relevant literature. Additionally, reputable journals in the field of computational acoustics and acoustics were targeted. Initial screening was performed by reviewing titles and abstracts to identify studies relevant to the research topic. Full texts of potentially relevant articles were then retrieved and reviewed in detail. Articles focusing on unrelated topics or lacking substantial contributions to the research questions were excluded. Selected literature was critically analyzed to extract relevant information on theoretical foundations, methodological approaches, and findings. Emphasis was placed on finding prior art and best practices for simulation modeling. Findings from the literature were compiled to provide a coherent background for the study, ensuring that the developed simulation model was well grounded. Key insights were integrated into the methodology, guiding model development and the planning of the experimental validation processes.

3.2 Overview of computational methods

The development of the simulation model was done from a blank model. The first phase was to learn the basics of COMSOL Multiphysics, and the thorough review

of the Acoustics Module User's Guide [23], specifically the documentation on transient and time explicit acoustics. Official tutorial videos, and step-by-step tutorial documents were the primary sources of information. For guidance and verification of the model setups, COMSOL Support was contacted twice.

The workflow for constructing and running a numerical model involved several steps, including cataloging and indexing the model, identifying suitable modeling methods, and selecting the domain type and physics interfaces. Additional steps included defining simulation parameters, manually configuring the solver if necessary, and defining outputs to be saved, along with constructing or importing geometry, assigning physics interfaces, defining material parameters, and assigning initial and boundary conditions. The final steps were meshing the geometry, verifying the solution of initial time steps, uploading the model to the Vera compute cluster if needed, queuing the simulation, downloading the finished simulation, post-processing and saving figures and data, and saving the model to a backup drive.

3.2.1 Meshing

A sufficient resolution of the mesh is a requirement for a model to able to accurately simulate any physical phenomenon. In COMSOL Multiphysics, there are two ways of generating a mesh. In user-controlled mesh generation, the user has direct control over the mesh parameters, such as element size, type, and distribution. This approach allows for customization to ensure fine mesh in areas of interest or high gradients, e.g. focal spots. Coarser meshes can be used in areas of lower expected gradients. However, this is time consuming and carries a risk of mistakes being made. Physics-controlled meshing, on the other hand, automatically generates the mesh based on the physical phenomena being modeled. The maximum frequency to resolve can be specified for different domains. The software adapts the mesh density according to the solution's requirements, ensuring sufficient resolution where needed. This approach simplifies the process for the user.

3.2.2 Adaptive meshing

In the case of a large domain and temporally limited source pressure wave, i.e. a tone burst pulse or a pressure pulse, it can be motivated to use a dynamic meshing scheme. The mesh is refined, based on specified refinement criteria, also referred to as error indicators. It is recommended to use the norm of the gradient of the pressure as the error indicator, as sharp gradients imply high amplitudes and the presence of multiple frequency harmonics in the signal. It is crucial that the mesh always is able to resolve the fundamental frequency, i.e. the source frequency. The minimum element size should not be less than $\lambda/1.5$. Note that this is way larger than the recommended element size of approximately 12 elements per wavelength, when using a static mesh. It is important to consider that a signal with a constant frequency has different wavelengths in different media.

Adaptive meshing allows for a *much* coarser mesh, which is refined only where the

acoustic pressure wave is located spatially. The mesh is updated at a few occasions during the simulation. This can save very large amounts of memory, up to orders of magnitude. Examples of estimates of numbers of mesh elements for different simulation setups are presented in Table 3.1.

Simulation type	**Geometry**	**Elements**
Fundamental frequency, static mesh, 2 MHz	15 mm cube	1.38×10^{7}
Third harmonic, static mesh, 2 MHz	15 mm cube	3.73×10^{8}
Eighth harmonic, static mesh 2 MHz	15 mm cube	7.08×10^{9}
Fundamental frequency, static mesh, 2 MHz	50 mm cube	5.12×10^{8}
Third harmonic, static mesh, 2 MHz	50 mm cube	1.38×10^{10}
Fifth harmonic, static mesh, 2 MHz	50 mm cube	6.40×10^{10}
Adaptive meshing, 2 MHz initial mesh, 2MHz	50 mm cube	1.00×10^{6}
Adaptive meshing, 2 MHz, 5th harmonic at 5% of domain	50 mm cube	3.21×10^{9}
Fundamental frequency, static mesh, 2 MHz	15 mm square	5.76×10^{4}
Third harmonic, static mesh, 2 MHz	15 mm square	5.18×10^{5}
Eighth harmonic, static mesh 2 MHz	15 mm square	3.69×10^{6}
Fundamental frequency, static mesh, 2 MHz	50 mm square	6.40×10^{5}
Third harmonic, static mesh, 2 MHz	50 mm square	5.76×10^{6}
Fifth harmonic, static mesh, 2 MHz	50 mm square	1.60×10^{7}
Adaptive meshing, 2 MHz initial mesh, 2MHz	50 mm square	1.00×10^{4}
Adaptive meshing, 2 MHz, 5th harmonic at 5% of domain	50 mm square	2.18×10^{6}

Table 3.1: Examples of numbers of elements included in mesh for different geometries and mesh settings

The number of degrees of freedom (DoF) solved numerically by the computer are given by the formula (number of DoF) = (number of mesh nodes) × (number of dependent variables). The NATE interface of COMSOL Multiphysics has 4 dependent variables, corresponding to scalar pressure and 3 wave velocity components. Although DGFEM, discussed in Subsection 2.5.4, is relatively memory efficient, memory quickly becomes the limiting factor as domain size increases, especially in the case of three-dimensional models. Naturally, the number of mesh elements increases with a power of 2 of the domain size in the case a 2D simulation, including axisymmetric geometries, and a power of 3 in the case of a full three-dimensional simulation. However, adaptive meshing was proven time consuming to implement, with crashing being a recurring problem.

3.2.3 Adaptive time stepping

As well as varying the resolution of the spatial discretization, the temporal resolution can be refined locally as well. The solver updates the time steps so that the

Courant–Friedrichs–Lewy condition is fulfilled [14], [23]. This relates the spatial resolution to the required temporal resolution for the convergence of the solution. This condition implies that an increase in spatial resolution must be followed by an increase in temporal resolution. This has the intuitive interpretation that the time steps must be shorter than the propagation time to adjacent mesh nodes. In NATE, this is implemented by changing the solver to *Adam-Bashford 3, Local*. However, doing so prevents certain couplings of different physics interfaces such as *Acoustic-Structure Boundary*, constraining the exciting boundary condition to a uniform time-dependent pressure boundary condition. It was noted in a late stage of the project that the similar multiphysics coupling interface - *Pair Acoustic–Structure Boundary, Time Explicit* allows for coupled models with local mesh based time step lengths.

3.2.4 Truncation of the simulation domain

As to limit the size of the simulated geometry, the domain has to be limited. However, as not to get reflections or artefacts from the boundary of the model, it has to be truncated in an appropriate way. For the NATE interface, geometries should be truncated by assigning boundary domains as absorbing layers. These are based on frequency filtering, slowdown of the incident wave and simple non-reflecting boundary conditions. These are recommended to be around 3 mesh elements thick to function properly. In the *Elastic Waves, Time Explicit* interface, a *Low-Reflecting Boundary* is recommended.

3.2.5 Running on compute nodes

The computations were enabled by resources provided by Chalmers e-Commons at Chalmers. A node of 32 processor cores and 96 GB of memory was made available at the Vera cluster. An execution script was written in the Bash shell language. Models were generated locally, and transferred to and from the cluster using *Secure copy protocol* tools.

3.2.6 Evaluation of delivered acoustic energy to tissues

To compare the results of simulations with values found in medical studies, such as EFD and PPP, the resulting pressure waveform must be inspected. By utilizing the tool *Domain point probe* in COMSOL, a time plot of any dependent variable, e.g. pressure, is generated. The temporal resolution of this plot is equal to the time steps of the solver, as opposed to the output time interval. The latter determines the interval of saving the entire state of the model at a given time step. This time series data can be inspected using tools integrated in COMSOL, or exported for further analysis, such as numerical integration for finding EFD.

3.3 Modeling of piezoelectric transducer

The modeled piezoelectric transducers were similar to the prototype hardware. They had a disk-like geometry, and consisted of PZT. The transducer disks were modeled and simulated without any acoustic coupling, as to analyze their resonant properties.

3.3.1 Material modeling

To obtain a full set of material values for the PZT disk transducer used in the early prototypes, the limited material datasheet was compared against table values for different PZT materials [27], provided by an commercial manufacterer. The background for this was that no detailed material datasheet was supplied for the actual hardware. The comparison with these table values [27] indicated that the material used in the sensor was a close fit to PZT-5A. The material was modeled as PZT-5A in simulations, by specifying the material as the predefined material PZT-5A in COMSOL. However, as a list of material properties was compiled in the closing phase of the project, it was noted that the material properties listed by COMSOL Multiphysics showed significant discrepancies with the aforementioned table values. It was decided not to change the modeled material, as not to prevent comparisons with previous simulations. However, this invalidates the direct comparison between the experimental work and the numerical model to some extent. The material parameters are listed in Section 4.1.

To align the polarizing direction of the material with the applied electric field, the coordinate system of the piezoelectric material was specified as the XZ-coordinate system, which is also the default option in the 2D-axisymmetric geometry.

3.3.2 Frequency response

The frequency response of the disk-shaped piezoelectric transducer was investigated in COMSOL Multiphysics, using a time-explicit simulation, with the *Solid Mechanics* interface. The piezoelectric disk was modeled as an axisymmetric rectangle, with diameter and height 5 mm and 1 mm respectively. The material parameters were set to those of PZT-5A. The backing was set to the same material, as to easily ensure the same acoustic properties. The dimensions of the backing material was set to 3 times that of the transducer disk, as to ensure that the non-reflecting boundary condition *low-reflecting boundary* could resolve the waveform. The domain material model *Piezoelectric material* was applied to both the backing material and the transducer disk. However, the piezoelectric dynamics were disabled for the backing material, by entering the coupling matrix manually as zero for all tensor elements.

The disk was excited by single short ($t_e = 0.25$ µs) period of a triangle wave with a voltage of 100 V. This was chosen to be much shorter than a period of observed resonance frequencies in previous simulations. This external field was applied as equipotentials on the surfaces corresponding to the metallized surface electrodes on the PZT element. The rear electrode was assigned a voltage of 0 V, i.e. it was

modeled as a ground plane. The simulation time was set to 100 µs, or approximately 50 oscillation periods, as to allow the spectral analysis to get a sufficiently fine FFT frequency bin width, which is inversely proportional to the length of the time series. The mesh was specified as a physics controlled mesh, able to resolve frequencies of up to 10 MHz. The simulation was run on a local computer, as the small domain size implied a low requirement on both CPU capacity and memory availability.

3.4 Modeling of 1D nonlinear acoustic propagation

A one dimensional model of nonlinear acoustic propagation was simulated. It was implemented in COMSOL Multiphysics, using the interface *Pressure Acoustics, Transient*, as the preferred interface NATE is not available in a one-dimensional computational domain. Guidance for this model was given through the COMSOL tutorial "Nonlinear Acoustics — Modeling of the 1D Westervelt Equation". The parameters used are listed in Table 3.2. The fluid model "general dissipation" was used to model the attenuating properties of the propagation medium, as per equation 2.17. The simulated propagation medium was chosen as muscle, due to its acoustic properties being similar to those of multiple types of soft tissue, as well as it constituting much of the soft tissue between the heart and skin.

The geometry was defined as an interval from 0 to 10 cm, representing the simula-

Variable	**Value**	**Description**
P_0	$[1, 3, 10, 30] \times 10^5\,\mathrm{Pa}$	Source pressure amplitude
f_0	$5 \times 10^5\,\mathrm{Hz}$	Source frequency
β	4.25	Coefficient of nonlinearity
c_0	$1588\,\mathrm{m/s}$	Speed of sound
ρ	$1081\,\mathrm{kg/m^3}$	Density
μ_0	$0.3\,\mathrm{Pa \cdot s}$	Viscosity
δ	$\frac{4}{3}\frac{\mu_0}{\rho_0}$	Diffusivity of sound
L	$0.1\,\mathrm{m}$	Computational domain length
N_0	8	Number of harmonics to resolve

Table 3.2: Parameters and descriptions for the one-dimensional nonlinear acoustic propagation simulation

tion domain. The nonlinear acoustics (Westervelt) contributions were added to the domain, with the coefficient of nonlinearity specified. Shock-capturing stabilization was enabled with q-Laplacian relaxation to handle shock formation. Boundary conditions were applied, with a sinusoidal pressure source at $x = 0$ and a plane wave radiation boundary condition at the far end of the domain, to model wave propagation without reflections. The mesh was generated using the physics-controlled mesh functionality, ensuring sufficient resolution of harmonics up to 8 times the fundamental frequency, as signs of shock formation was observed in previous simulations

at similar conditions.

The study settings were configured with appropriate output times, and the simulation was executed on the Vera cluster, in order to save time. Results were analyzed by plotting the acoustic pressure at various points along the domain. Cut points were created to facilitate this comparison, and frequency spectra were plotted to examine the harmonic content of the propagated wave.

3.5 Modeling of a focused acoustic transducer

With the guidance of the tutorial *High-Intensity Focused Ultrasound (HIFU) Propagation Through a Tissue Phantom*, an axisymmetric model of a spherical acoustic transducer, emitting a tone burst pulse propagating towards a focal point was created from a blank model. The model setup began with the definition of the model geometry and signal. The geometry was parameterized, to easily perform changes in a later stage. Global parameters, including source pressure amplitude, frequency, and material properties like speed of sound and density for water and tissue, were defined. These are listed in Table 3.3 A spherically focused ultrasound transducer with a concave lens was constructed. The transducer emitted a five-cycle tone burst with an amplitude of 0.1 - 0.25 MPa and a center frequency of 1 MHz. The geometry configuration involved creating a circle representing the lens radius and rectangles to define regions for water, tissue, and absorbing layers for truncating the domain with non-reflecting boundaries. An analytic function was defined for the pulse signal, incorporating sinusoidal functions to represent the tone burst.

Mesh generation was carried out using a free triangular mesh with element sizes of $\lambda/1.5$ to resolve the fundamental harmonic of the signal. Adaptive mesh refinement was enabled to automatically refine the mesh locally around the propagating signal, as per Subsection 3.2.2. The physics setup involved applying the Nonlinear Pressure Acoustics, Time Explicit model to the entire defined geometry. Boundary conditions for material discontinuities at the water-tissue interface were set, along with pressure and impedance conditions. Domain point probes were placed at the water/tissue interface and the focal point to record the signal during propagation. Absorbing layers were set up to truncate the computational domain and prevent reflections. The solver configuration used the Adams-Bashforth 3 (local) time-stepping method for the explicit solver, ensuring convergence with respect to the Courant–Friedrichs–Lewy condition.

The simulation was then executed for the defined time range. The results were analyzed to examine signal propagation, focusing effects, and frequency content. Plots of relative pressure probes, frequency spectrum, and other relevant parameters were generated to evaluate the nonlinear propagation characteristics. This systematic approach ensured accurate simulation of HIFU propagation through a tissue phantom, capturing essential nonlinear effects and signal behaviors. The use of adaptive meshing and explicit time integration facilitated efficient and precise modeling of complex acoustic phenomena.

Parameter	Value	Description
P_0	0.25 MPa	Source pressure amplitude
f_0	1 MHz	Source frequency
α_{water}	0.025 1/m	Absorption coefficient of water at 1 MHz
α_{tissue}	8.55 1/m	Absorption coefficient of tissue phantom at 1 MHz
c_{water}	1484 m/s	Speed of sound in water
c_{tissue}	1568 m/s	Speed of sound in tissue phantom
ρ_{water}	1000 kg/m^3	Density of water
ρ_{tissue}	1044 kg/m^3	Density of tissue phantom
B/A_{water}	5.2	Parameter of nonlinearity of water
B/A_{tissue}	7.4	Parameter of nonlinearity of tissue
δ_{water}	$2\alpha_{\text{water}}c^3_{\text{water}}/\omega_0^2$	Sound diffusivity of water
δ_{tissue}	$2\alpha_{\text{tissue}}c^3_{\text{tissue}}/\omega_0^2$	Sound diffusivity of tissue phantom
F	60 mm	Focal length
r_{source}	62.64 mm	Lens radius
w_{source}	35 mm	Lens aperture
z_{tissue}	24.6 mm	Starting position of tissue phantom
h_{model}	95.1 mm	Total height of the model
r_{model}	43.6 mm	Total radius of the model
th_{abs}	5 mm	Thickness of the absorbing layer

Table 3.3: Parameters and their descriptions for the model of the spherical focused transducer

3.6 Modeling of the human body

The material properties of modeled tissue were taken from the Virtual Population project of IT'IS, ETH Zürich [24]. Values for the nonlinearity parameter, density, speed of sound and attenuation coefficient were available. The attenuation coefficient α was converted to diffusivity δ using the formula

$$\delta = 2\alpha \cdot c^3/\omega_0^2, \tag{3.1}$$

where ω_0 is the angular frequency at which α was measured.

The anatomical model *Duke* from the same source, Virtual Population project of IT'IS, was downloaded, and imported into COMSOL Multiphysics. The model was based on segmented magnetic resonance images of a 34 year old, 177 cm tall male. The model consisted of Standard Tesselation Language (STL-) files. Each tissue type was represented as its own file, containing three-dimensional objects, which could be imported directly into the mesh in COMSOL.

These objects required significant processing in order to form watertight domains. Each object was not necessarily connected, and some objects were not watertight, i.e. the tesselation surface was not closed. The built-in tools of COMSOL were employed to repair and modify the mesh, as shown in Figure 3.1. This was very

time consuming, and consisted of the following suboperations:

- Positioning of each STL object
- Partition of the whole-body model into a manageable volume
- Closing the boundaries of the objects to closed surfaces
- Deleting self incident faces and reconstruction of surfaces
- Deleting faces adjacent to self intersecting edges
- Generation of domains from closed surfaces
- Generation of a void-filling domain
- Joining the different domains in a meshing sequence
- Forming a union of the domains, i.e. joining their boundaries
- Repair of overlaps and voids
- Remeshing the domains with a suitable mesh resolution, as per Section 3.2

A manageable domain size, from a mesh handling perspective, that allows modeling of different regions of the anterior chest wall and cardiac tissue was assessed to be a cylinder with a height of 125 mm, and a diameter of 140 mm. The symmetry axis of the cylinder was aligned with the normal vector of the frontal plane of the model, i.e. the front face of the cylinder was approximately aligned with the skin of the chest. The symmetry axis was placed approximately 3 cm left of the sagittal plane, 5 cm above the processus xiphoideus, i.e. the lowest part of the sternum. These values approximately centered the cylinder at the center of the heart.

The downloaded model contained an 3D object referred to as ”other tissue”, which was a non-connected void filling domain, consisting of hundreds of closed surfaces generated by the original segmenting software. This object was not included, as to minimize the number of domains. Instead, the following domains were generated as previousy described:

- Heart (entire cardiac muscle)
- Lungs
- Bone (sternum)
- Cartilage (costal cartilage)
- Liver
- Skin (3 mm)

As some voids remained, a conical shape was defined, extending and widening in the dorsal direction from the skin. This shape was defined as ”general soft tissue”, which was assigned the material properties of muscle.

As the 3D objects were imported directly into the mesh, it was not feasible to truncate the domain in the typical way, which is through adding a layer to the geometrical objects and specifying it as an absorbing layer as discussed in Subesection 3.2.4. Instead, an artificial domain in the shape of a hollow cylinder had to be constructed through manual manipulation of the mesh, and designated as an absorbing layer.

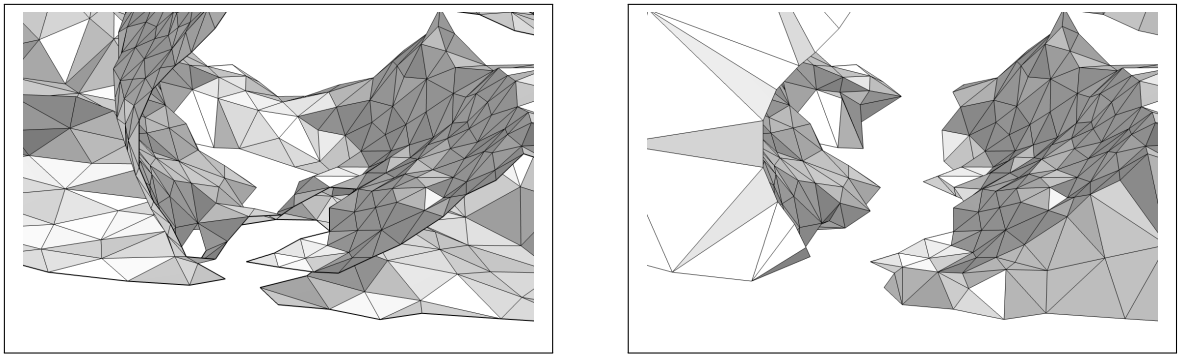

(a) Broken, open mesh **(b)** Repaired, watertight mesh

Figure 3.1: Repair of the mesh of the muscular tissue surrounding a rib

As a simulation geometry with watertight domains were formed, it was tried to run simulations of acoustic propagation. Boundary conditions and simulation parameters were introduced, with values similar to other models. This resulted in multiple error messages, and repeated crashing. Out-of-memory errors could be resolved with limiting the size of the geometry to a smaller cylinder measuring 40 by 40 mm, and reducing the mesh fineness and simulated frequency. Implementing adaptive meshing resulted in crashing without exception. Implementing a static mesh resulted in errors regarding problem stiffness, i.e. exceedingly small timesteps required by the solver. Despite much time being allocated to this, these problems were never solved, and no simulations were run.

3.7 Coupled modeling of acoustic field and transducer

In order to model a complete coupled system with both a wave propagation medium, and a piezoelectric transducer element, a simulation model was developed. The geometry was axisymmetric, and the physics interfaces for NATE, electrostatics and *Elastic Waves, time-explicit* were used. The aim of the simulation was to demonstrate that the performance of different transducer geometries could be simulated and evaluated. The geometry consisted of a 5 mm wide, 1 mm high disk of PZT-5A, with boundaries corresponding to the metallized surface. In the domain of the disk, the Electrostatics and Elastic Waves interfaces were applied. In the propagation medium domains, the NATE interface was applied. The interaction between these physical solvers were handled by the Multiphysics interfaces ”Piezoelectricity” and ”Acoustic-Structure Boundary”. The meshing was static and physics-controlled, resolving up to 5 MHz. The propagation medium consisted of several layers of tissue types: a skin layer of 3 mm, a fat layer of 12 mm and a muscle layer of 20 mm. The domain was truncated with a hemispherical absorbing layer domain, with an inner radius of the sum of these thicknesses. This radius was later reduced to 22 mm, as to save computation time when evaluating different backing types. This is shown in Figure 3.2.

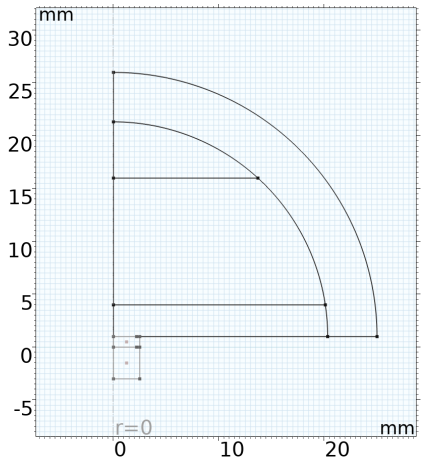

Figure 3.2: Geometry of coupled piezoelectric-acoustic simulation

This model allowed for inspection of the beam spread angle, investigations on the influence of backing, influence of the driving voltage, inspection on maximum tensile forces in the transducer material, as well as analysis of the generated PPP and EFD.

3.8 Experimental methods

The available measurement equipment was limited to thin polyvinylidene fluoride (PVDF) film sensors and PZT sensor disks. These were applicable for simple measurements, but had some drawbacks. As the sensing area was an order of magnitude larger than the wavelength of the transmitted signal, multiple periods of a waveform would be sensed if the incidence angle was very small. Even needle hydrophones with small sensing apertures exhibit a strong correlation between the ratio between wavelength and sensing surface diameter, and sensitivity at different angles of incidence. Further, these sensing elements were not calibrated, and had problems with reliably detect the small acoustic pressures achieved by the available equipment. It was suspected that the PZT sensor disks have a non-uniform frequency response, with high sensitivity at resonance frequencies and the opposite at anti-resonance frequencies. The PVDF film sensor was suspected to have a high capacitance and hence a low cut-off frequency, as well as issues with directivity.

However, some simple measurements were made with the PVDF film sensor. The driving circuit used was an Agilent 33220A arbitrary waveform generator, operating at its maximum output voltage of 10 V peak-to-peak. The driving signal was a square wave, at a frequency of 100 Hz. This was chosen so that the period of the signal was much longer than the ring down time, and no thermal issues arose with the transducer disk. The transmitting disk was air-backed and coupled to the polyurethane tissue phantom block with ultrasound coupling gel. On the opposite side of the block, the PVDF film sensor was coupled similarly. The sensor was connected to an SR560 low-noise preamplifier, manufactured by Stanford Research Systems, with settings optimized for suppression of noise. The preamplifier, as well as a synchronization signal cable from the driving signal generator was connected

to a digital oscilloscope.

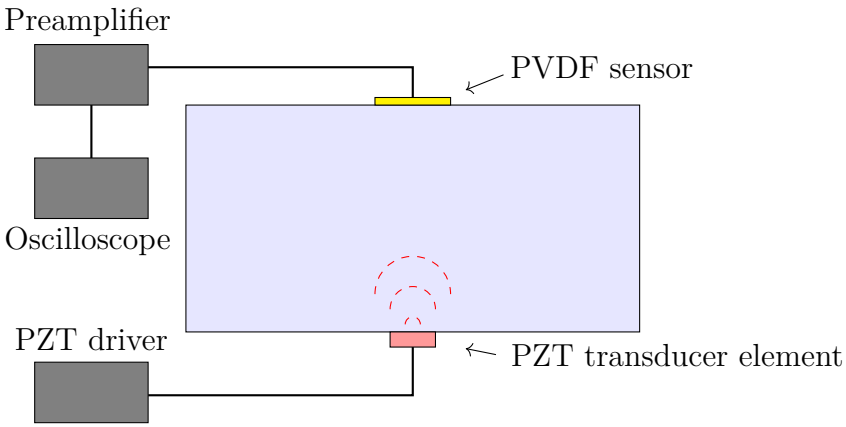

Figure 3.3: Schematic of the PVDF film pressure sensor measurement

3.8.1 Construction of PZT element holder

A design was developed for holding multiple PZT elements, specifically of the model *Z050 A 206 A 31* manufactured by TDK. The holder was designed in Autodesk Inventor, and constructed in polyethylene terephthalate glycol (PETG) using additive manufacturing. The threads were cut using taps and dies. In order to arrange the transducers in a quadratic grid array configuration of 4 by 4, with dimensions 36 mm by 36 mm, i.e. the center-to-center distance between transducer elements being 12 mm, a jig was designed and manufactured similarly. This jig is shown in figure 3.5.

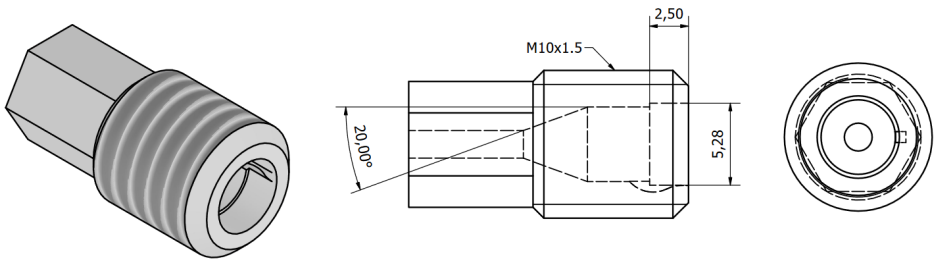

Figure 3.4: Drawing of the PZT element holder, with dimensions in mm

The design of the PZT holder was made with some considerations and features. The front recession was to hold the PZT element, as well as a polymer coupling layer. These were to be joined by gluing, with a glue with similar stiffness and density, i.e. the same acoustic impedance Z, to the coupling layer. The depth of the recession

was set to 2.5 mm, as the thickness of the element was 1 mm, and the wavelength of the signal in acrylic was expected to be around 2.7 mm, giving a value of $3\lambda/4$ of 2.05 mm for maximizing the transmission. The latter value was based on the speed of sound in acrylic plastic, and observed resonance frequency, of the PZT element when in contact with a silicone tissue phantom, coupled with ultrasonic coupling gel. The values on resonance frequence are presented in Section 4.6. Acrylic was chosen for its ease of manufacturing, availability, and its high acoustic impedance - about 3.3 MRayl - relative to other polymers. The optimum coupling layer impedance between skin (1.8 MRayl) and PZT (33 MRayl) is around $\sqrt{Z_1 Z_2} = 7.7$ MRayl. Despite the discrepancy between the optimum and the chosen material, the coupling layer was expected to increase the transmitted power.

The coupling layer was also intended to work as a wear plate, reducing cavitation induced erosion of the only 5 µm metallization of the PZT element. Tuning of the thickness of the damping mateiral was to be done through grinding of the coupling material. For ease of assembly and on-site repairs in the laboratory with limited time, the element array was designed to work in a modular principle. The element holders were threaded, and a hexagonal shaft with a width of 7 mm was included, intended for manipulation with a standard open ended spanner.

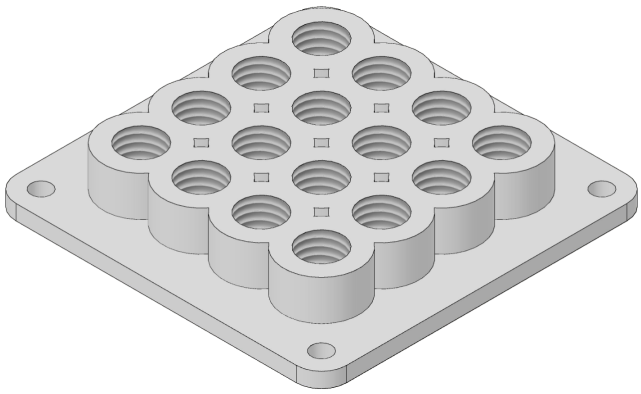

Figure 3.5: Computer rendering of the PZT element holder array jig

The transducer was designed in order to allow for the implementation of backing material in the transducer. The rear opening was wide enough to allow the cavity behind the PZT element to be filled with epoxy, through a syringe. It would be crucial that no air voids be present. Ideally, this backing material should have the same value of Z as PZT. Commercially available tungsten powder was to be mixed with epoxy glue to achieve this. The rear cavity of the transducer was designed with a taper angle of 20°. This design has the effect of enabling multiple reflections of the waves transmitted from the rear face of the PZT element, dissipating the energy and minimizing standing waves, hence giving the transducer a more uniform frequency response. Copper wires with 0.1 mm diameter were stripped of their insulating layer and attached to the PZT element using conductive glue. This small diameter was chosen as to minimize the mass coupled to the element, which influences its resonant frequency, while still providing some mechanical robustness. The wires were routed

back through the rear opening of the element holder. These would be robustly attached to the transducer unit by the internal tungsten-epoxy backing. As to reduce emission of electric noise and interference, the two wires were joined as a twisted pair. The resistivity of one of the wire strands was calculated to be approximately 2.2 Ω/m, which yielded a RC-circuit time constant of under 1 ns, which is negligible relative to the mechanical inertia of the system.

Due to the planned experiments at Lund University and the purchase of a needle hydrophone being cancelled, the development of the PZT element holder was put on hold and limited to the design, and construction of a few prototypes without backing or coupling layers.

3.8.2 Design of experiment setup

Experiments to be performed at Vattenhallen Science Center, Lund University were designed and planned. The reason for planning the experiments at Lund University, was that both Chalmers and RISE AB in Gothenburg and University West in Trollhättan, lacked the industry standard measurement instruments for pressure field mapping, i.e. needle hydrophones. These devices are suitable for pressure measurements with a very high spatial resolution, which is instrumental when the wavelength of the measured waveform is on the order of millimeters, or sub-millimeter.

Based on literature reviews, inventory lists and technical specifications, an experimental setup was developed. The goal of the experiments would be to vary the driving voltage of the transducer array, and observe the waveforms, possibly identifying effects from nonlinear acoustic propagation, such as shockwave formation and its dependence on input power and propagation distance. Effects such as constructive interference and the radiation patterns of the transducer elements would also be investigated.

The experiment would be split into two parts - one utilizing more conventional measurements techniques, and one more experimental. The first one would consist of submerging a transducer unit into a tank. The tank would be filled with degassed and pure water, as to minimize the risk of inertial cavitation damaging the needle hydrophone, which has a fragile PVDF sensing tip. The transducer array would be fixed statically to a jig. The hydrophone would be attached to a stepper motor system, allowing for both precise translation and alignment of the hydrophone with the acoustic propagation axis, i.e. approximately radial to the transducer if using a single element. The stepper motor system would be controlled programmatically through a computer, allowing for spatial mapping of the pressure field, and comparison with simulations.

The transducer elements were to be driven by either an H-bridge switching driving circuit or a Texas Instruments TX75E16EVM piezoelectric driver evaluation board, connected to a personal computer running appropriate software. This driving circuit can drive 16 piezoelectric elements in a single-ended configuration, with

a 5-level quasi sine wave up to ±100 V. These channels can be accurately and arbitrarily delayed, allowing for easy implementation of focal steering, which would be investigated. If focal steering through electronic delay was to fail, the design of the jig would allow for manual focusing by positioning each element on the surface of an imaginary sphere with its center at the desired focal point.

The second experiment setup design is shown in Figure 3.6. It would consist of a solid gel tissue phantom with drilled holes. These holes would be filled from the bottom with coupling gel, or other liquid with a similar acoustic impedance to the phantom material. It would be crucial that these holes be filled without gas bubbles entering. A lower viscosity liquid could mitigate this problem. The tissue phantom would be placed on top of an array of transducer elements.

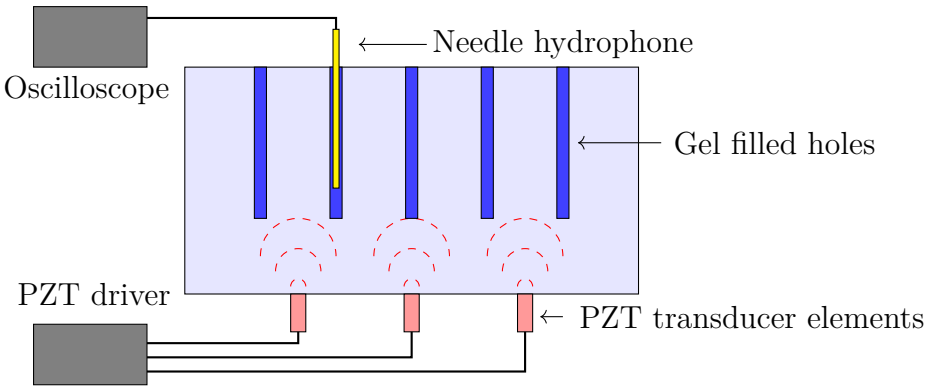

Figure 3.6: Schematic of the second planned experimental setup

The field would be mapped spatially as far as allowed by the constraints of the holes. The effects of different driving voltages and focal steering would be measured. This could be used for verification and tuning of the simulated model, as well as characterization of the available silicone tissue phantoms.

3.8.3 Selection of needle hydrophone

As the planned experiments at Lund University were cancelled due to high associated costs, the possibility of purchasing a needle hydrophone to RISE AB was investigated. Multiple models were considered, including but not limited to the product lineups of Onda Corporation, Precision Acoustics Ltd and Dr. Müller Instruments GmbH. The following aspects were considered and discussed with sales representatives:

- Frequency response
- The possibility of inertial cavitation
- Directivity at different frequencies
- Sensitivity
- PPP tolerance
- Spatial resolution, i.e. sensing element size

- Low interference with incident acoustic field
- The need for a preamplifier
- Instrument longevity
- Instrument calibration

After consideration, it was recommended that an Onda HNA-0400 needle hydrophone be purchased by RISE AB, as this instrument fulfilled the requirements on the aspects listed above. However, due to prohibitively high cost of the suggested instrument, a cheaper alternative was recommended for purchase. The selected instrument was a Müller-Platte Needle Probe, manufactured by Dr. Müller Instruments GmbH. Unfortunately, this purchase was also cancelled due to the seller not fulfilling requirements on vendors. After this, the project shifted to comprise a purely computational study.

4

Results

The primary goal and result of this thesis was the development of simulation procedures and techniques, presented in the previous chapter. This chapter will present simulation outputs of examples of possible simulations, as well as the results of the limited experimental work.

4.1 Transducer model

4.1.1 Material modeling

Initial comparison between commercial material datasheets and the specification of the TDK disk transducer indicated that its material was PZT-5A. This was based on the most relevant material parameters, i.e. the axial piezoelectric coupling coefficient e_{33}^{ES}, the axial stiffness parameter c_{33} and the material density ρ. The term axial implies that it specifies the coupling and stiffness in the direction of polarization, i.e. characterizing the performance of the transducer and its resonant properties. These values are shown in Table 4.1.

Property	TDK	PZT-5A*	-4D	-5A	-5H	-5J	-7A	-8
e_{33}^{ES} **(C/m^2)**	21.42	20.96	15.26	15.78	23.24	16.57	9.48	13.91
c_{33}^{E} **(GPa)**	51.0	53.7	128.2	110.9	117.4	59.8	125.7	131.7
ρ **(kg/m^3)**	7800	7950	7600	7750	7500	7400	7700	7600

* values from [27]

Table 4.1: Comparison of material properties from Datasheet and COMSOL Multiphysics library.

As mentioned previously, a mistake was made in not explicitly checking the material property parameters of the predefined materials in COMSOL. This resulted in a discrepancy between the material parameters of the piezoelectric transducer disk used in experiments, and those modeled in simulations.

4.1.2 Frequency response

As expected, we observe that the different types of backing have a large impact on the impulse response of the piezoelectric transducer in the frequency domain. The plots present the frequency spectrum of the average axial displacement of the front face of a free transducer, as described in section 3.3. In the case of the air-backed transducer, a large resonance peak is identified in the average displacement spectrum at $f = 400$ kHz. For the transducer with a fixed constrain on the rear face, interpretable as a backing with infinite acoustic impedance, the resonance frequency is around 600 kHz.

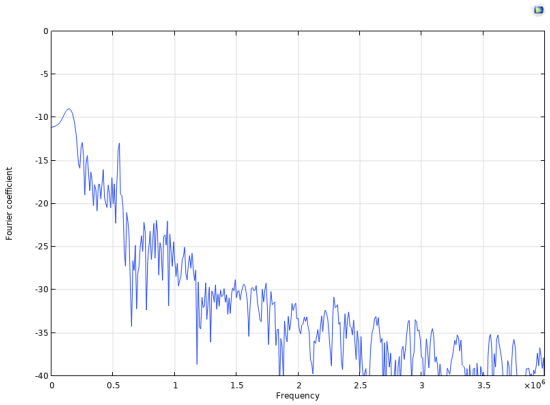

(a) Transducer with matched backing

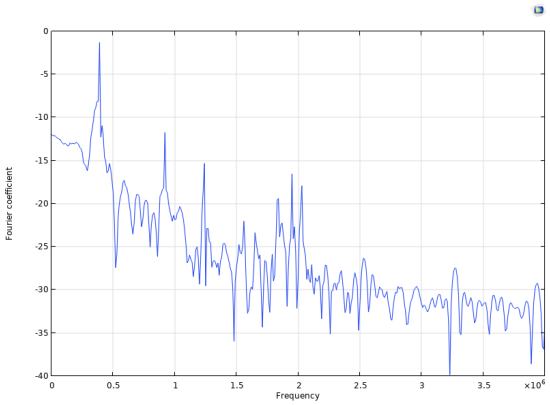

(b) Air-backed transducer

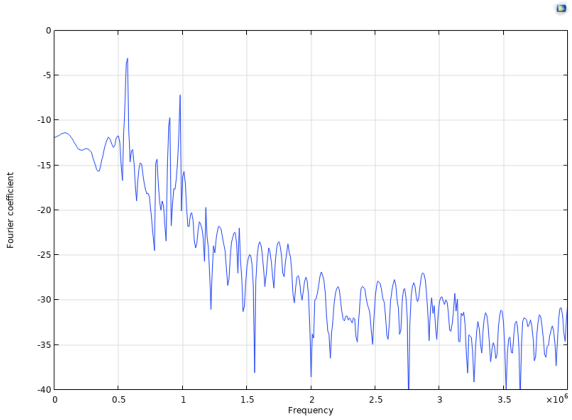

(c) Transducer with fixed rear face

Figure 4.1: Simulated pressure intensity spectra for different types of transducer backing

This indicates that a standing wave with $h = \lambda/2$ has formed in the free-face transducer and a standing wave with $h = 3\lambda/4$ has formed in the transducer with a fixed rear face, where $h = 5$ mm denotes the thickness of the disk, in both cases equating to an axial acoustic velocity of 4000 m/s, matching the expectations for the material [27]. The transducer with perfectly matched backing has a small resonance peak at close to 500 kHz. The low amplitude of the peak indicates a rapid damping of the oscillation of the transducer element.

4.2 One-dimensional acoustic propagation

Although a basic model, not considering the angular spread of the acoustic wave, but rather modeling a planar wave, a one dimensional model can provide insights in what signal distortion and attenuation one can expect. A nonlinear model was employed, and different inlet boundary pressure magnitudes were compared. The resulting waveform, as a function of distance from the pressure source is shown in Figure 4.2. A simple model with a homogenous propagation medium was chosen for this, as to minimize complexity and illustrate the tendency for waveform distortion for different materials at different frequencies and pressures.

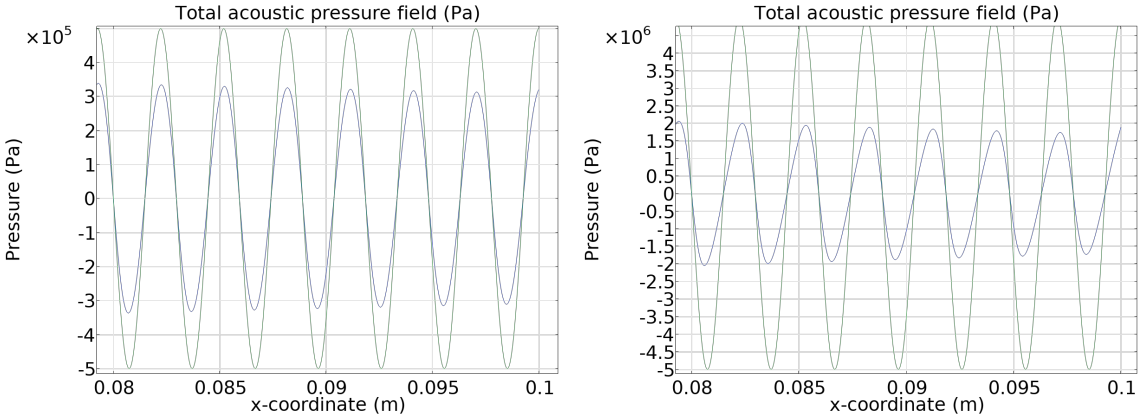

(a) Waveform at 0.5 MPa source pressure **(b)** Waveform at 5 MPa source pressure

Figure 4.2: Simulated waveforms with different source pressures after approximately 80 mm of propagation through a nonlinear medium

It can be seen in the plots that the waveforms are attenuated with increasing propagation distance. Note the different scales on the vertical axes. The higher amplitude signal has been relatively more attenuated, since the nonlinear effects have produced harmonics which are more rapidly attenutated. Also note the steepening of the wavefront of the signal with the 5 MPa source. This is expected, as nonlinear effects increase with the pressure gradient magnitude.

4.3 Coupled transducer element model

The simulation models where the piezoelectricity and NATE physics interfaces were coupled yielded interesting results, where several phenomena could be identified. The -6 dB beam width of a transducer element was analysed, which is shown in Figure 4.3.

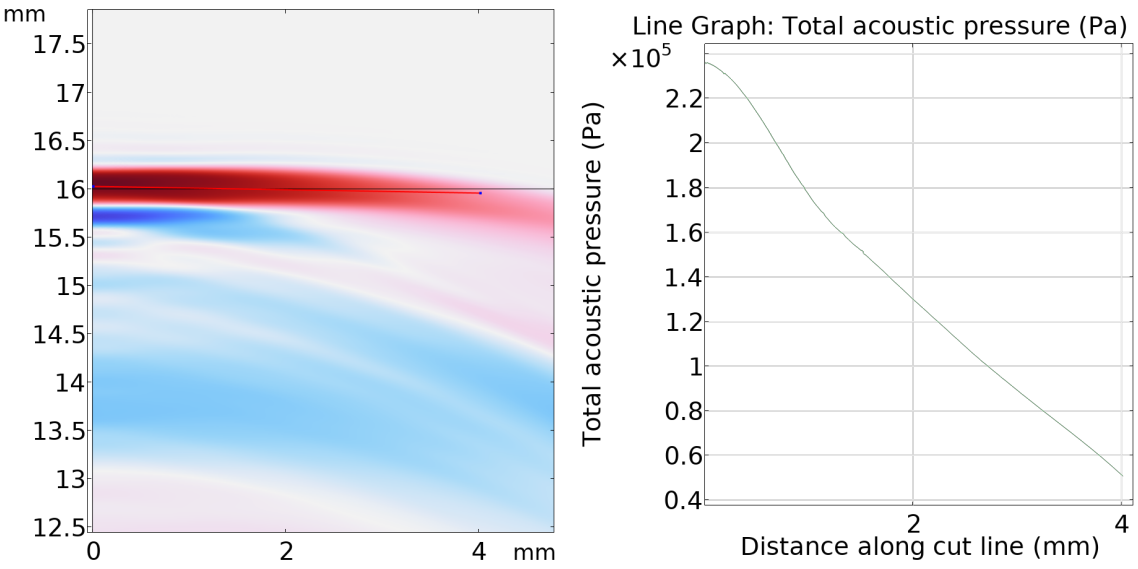

(a) Line along which pressure is plotted **(b)** Pressure along cut line

Figure 4.3: Beam width analysis at z=16 mm, showing cut line in relationship to the pressure wave at a given time step, and pressure amplitude along the cut line

It can be seen that the -6 dB beam width, i.e. the diameter of the beam at which the pressure is half of that at the center is found at approximately 4.6 mm ($r = 2.3$ mm) at a propagation distance of 15 mm from the transducer front face. Analysis of these values as a function of propagation distance can provide insight on the beam pattern of a transducer element, which is crucial when designing a focused transducer. The measured -6 dB beam spread angle is less than 5.4° from the center axis, limiting the achievable focusing direction of any planar steerable array constructed from the modeled elements.

The time domain signal of the acoustic pulse, measured at the symmetry axis at $z = 10$ mm, is presented in Figure 4.4.

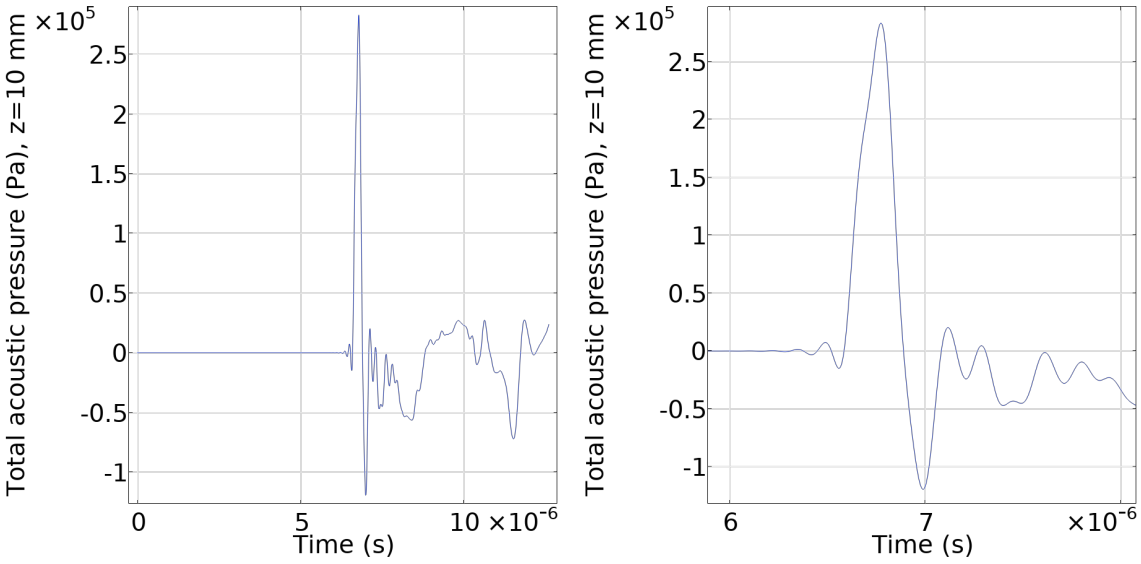

(a) Waveform of signal

(b) Detail of waveform of signal

Figure 4.4: Simulated pressure time series generated by a 300 V voltage step applied to a backed transducer

It is noted that the rise time of the pressure wave is approximately 200 ns, which is greater than the set voltage rise time of 125 ns. This long rise time was set to solve problems with the software crashing. A more physical value would be around 1 ns, based on the RC-circuit time constant $\tau = RC = 0.6$ ns, where R is the resistance of the wire, and C is the capacitance of the transducer, considering the driving circuit as an ideal voltage source. While it is clear that the step response is dominated by the mechanical inertia, rather than electrical phenomena, a shorter rise time should ideally be modeled. It is also noted that the pressure rise time is very close to a period length of the maximum resolvable frequency of 5 MHz. As previously discussed, shockwaves do not have a clear definition. However, this waveform shows the abrupt pressure gradients associated with shockwaves, even if it is in the upper range of rise times. A longer propagation distance steepens the wavefront.

The PPP is evaluated to 0.283 MPa. Analysis and numerical integration over the positive pressure pulse according to Equation 2.2 yielded a EFD of 6.86×10^{-6} mJ/mm^2. This is a discrepancy of over two orders of magnitude compared to the value that Equation 2.1 predicts, which is that a shockwave of that EFD has a pressure peak of only 0.0108 MPa. This is due to the very short peak observed in the simulation result. This illustrates the need to evaluate EFD and PPP separately.

4.4 Focused transducer model

The propagation of a tone burst pulse emitted by a spherical acoustic transducer was modeled. The adaptive meshing algorithm updated the discretization 10 times during the simulation. The refined mesh at a given time step and a corresponding surface plot of the time step length used by the solver are depicted in Figure 4.5.

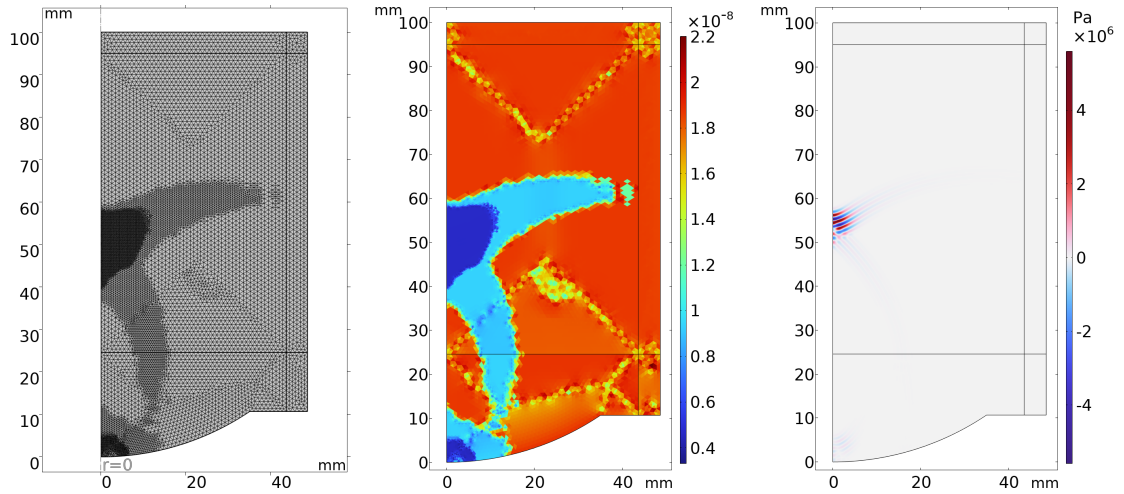

(a) Refined mesh **(b)** Solver time step length **(c)** Pressure surface plot

Figure 4.5: The refined meshed geometry, and solver time step length, and surface acoustic pressure plot at a given time step

It can be seen that the mesh is refined in the region surrounding the focal spot. This correlates directly with shorter time-stepping of the solver. Effects from diffraction, radiating from corners result in the mesh refinement being activated. After that the propagating wave has passed, the mesh is coarsened again, as well as the time step being made longer.

The pressure increased rapidly and inversely proportional to the volume containing a pressure peak of the signal. This volume decreased proportionally with the distance to the focal point, focusing into a spot with a size on the order of a wavelength. The focal gain, i.e. ratio of peak pressure to source pressure was observed to be over 90. The wavelength of the signal was 1.48 mm, and the diameter of the source surface 70 mm. This pressure increase, and subsequent decrease after the focal point has been passed, is shown in Figure 4.6. The pressures at times t =[10, 33, 45, 55] µs are visualized in blue, green, red and light blue, respectively. The distances and pressures in the figure are specified as relative values, normalized such that the distance to the focal point and the source pressure are both equal to 1.

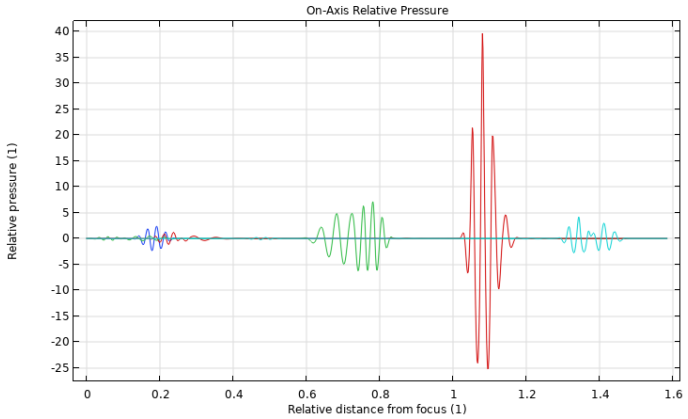

Figure 4.6: Relative pressures along the symmetry axis, at different time steps

While this model excites the modeled acoustic field through a pressure boundary condition, it would also be possible to model a spherically polarized piezoelectric shell. For it to be practically feasible, the meshing scheme must be changed to adaptive meshing, requiring the solver to allow for adaptive time-stepping, further calling for the coupling to be changed to *Pair Acoustic–Structure Boundary, Time Explicit*. Care must be taken when defining the coordinate system of the material, so that the polarizing direction of the material is defined radially from the focal point of the transducer. In practice, multiple smaller transducer elements would be placed on the spherical surface, to allow for focal steering. The spacing between these elements are not possible to model in an axisymmetric geometry, but an approximation employing a lower amplitude of the exciting signal could likely be used.

4.5 Anatomical model

The detailed anatomical model could not be used in simulations, as mentioned in Section 3.6. However, it was useful for visualizing the anatomy and defining simplified models of the relevant geometry. It can provide guidance in visualizing the acoustic window, i.e. the area in which an acoustic transducer can be placed for uninterrupted signal transmission to the heart. Although it is difficult to visualize a three-dimensional object in this form, this can be seen in Figure 4.7.

This visualization depicts the part of the thorax, partitioned by the cylinder mentioned in Section 3.6. The soft tissues, i.e. muscle, skin and generic soft tissue have been removed from the model. Aligned vertically, slightly to the left in the figure, the sternum can be seen. Extending out from the sternum, and slightly darker in color, the costal cartilage, i.e. the cartilagous parts of the rib cage, can be seen. To the upper right in the figure, the left lung is seen. The liver is located under the heart, to the left in the figure. Its boundary to the right lung is obscured by the costal cartilage. The heart is the rearmost structure, and is highlighted in blue.

The assignment of different domains is visualized in Figure 4.8. A unique color implies that a region has a closed surface, rather than having a specific material.

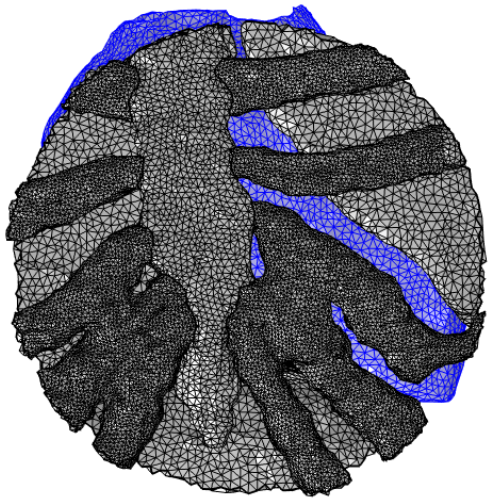

Figure 4.7: Anterior view of the used 3D model of the human thorax, excluding soft tissues except for the internal organs, with the heart highlighted in blue

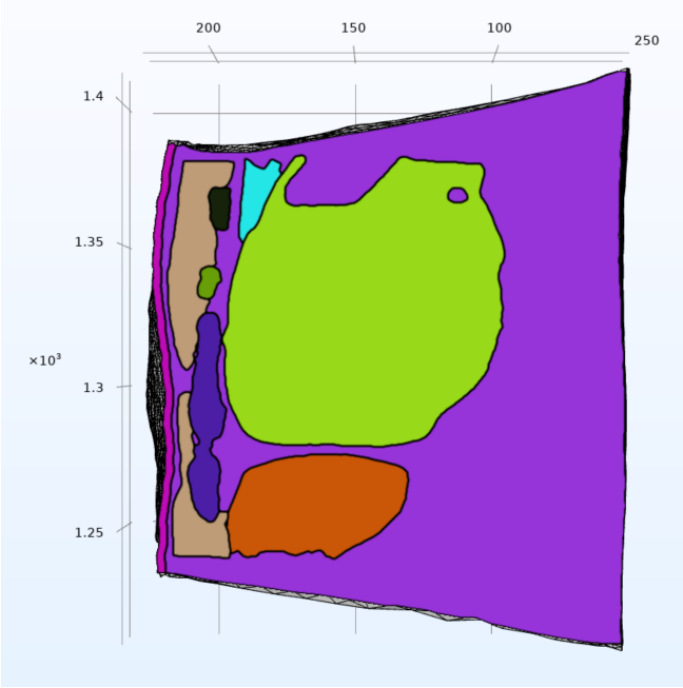

Figure 4.8: Cross section of three-dimensional anatomical model, with dimensions in mm

In the figure, the skin is colored pink, the pectoral muscle beige, the general soft tissue purple, the lung light blue, the heart light green, the liver orange and the different domains of costal cartilage are colored dark blue, green and black. A void, assigned to have the material properties of general soft tissue can be seen between the lower part of the pectoral muscle and the dark blue costal cartilage. The majority

of voids were repaired, but a few remained. This was deemed acceptable. The use of the general soft tissue domain made sure that all volumes were assigned a domain. The boundaries to domain-less volumes are automatically assigned as hard, perfectly reflecting, walls by the simulation software.

4.6 Experimental results

The experimental part of this project was limited, as no conventional measurement instruments were available. Still, the experiments detailed in section 3.8 provided some information on the step response of the piezoelectric transducer disk. The time series of the voltage generated by the PVDF film, and the corresponding power spectrum is presented in Figure 4.9.

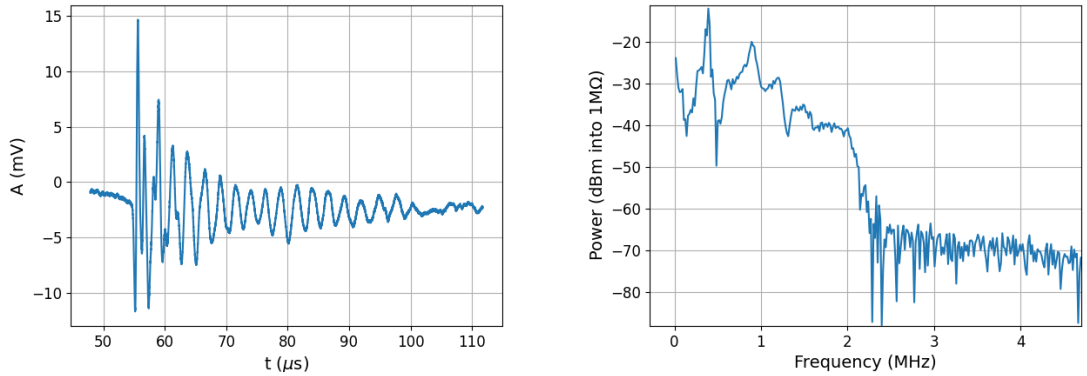

(a) Time series of output voltage **(b)** Frequency spectrum of output power

Figure 4.9: Experimental data on signal transmitted through a polyurethane gel block

The time on the horizontal axis is the time since the triggering of the output of the function generator, driving the piezoelectric element. The slope of the voltage remnant from the spike generated by the capacitive coupling can be seen at around t=50 µs. Two distinct phases in the waveform can be observed. The first phase consists of about two and a half wave periods, with high amplitude and a period of approximately 1.1 µs, corresponding to a frequency of about 0.9 MHz. After this, a ring down phase can be seen, drastically terminating at about t=100 µs. This ring down phase exhibits approximately half of the frequency of the first phase. This can indicate the transition between vibration modes, i.e. the transducer disk not simply oscillating axially. These distinct frequencies can be identified as peaks in the spectral power density plot. A discrepancy to the listed resonant frequency of the transducer disk, at 2 MHz, is noted. Instead, we see that the resonant frequency is similar to that found in Section 4.1, despite the different material parameters of the modeled and the actual transducer.

It is noted that assuming a linear relationship between voltage and pressure is likely not an accurate approximation due to two factors. As the propagation distance

differs about 0.4 mm, or close to a third of a wavelength at 1 MHz, between the center of a perfectly plane square 15 mm PVDF film sensor, and its periphery. This is due to the distance between the transducer and the sensor being 75 mm. As the film is flexible, the deflection is likely much larger than this, and is difficult to discern manually. Additionally, as the PVDF film sensor consists of a thin dielectric material between two electrodes, its capacitance is likely high, suppressing higher frequencies. This is a possible explanation for the sharp decline of the spectral power density at around 2 MHz, approaching a noise floor of -70 dBm.

5

Discussion

5.1 Accuracy of numerical models

As no experimental verification with calibrated instruments could be performed, it was decided not to try to verify and calibrate the model against these experimental values. However, areas where the simulated models differed from anatomical models were identified. Some tissues are not isotropic, e.g. muscle has an attenuation constant that differs significantly depending on propagation direction. Nor are all tissues homogeneous, as modeled. Boundaries between organs and tissues are not clear cut discontinuities, but instead have tissue layers separating them.

The points listed above do not constitute suggestions for improvement per se. Rather, the complexity of the model must be managed. For instance, the heart is surrounded by the pericardium, which in turn consists of the dense fibrous pericardium, and the serous pericardium. The latter secretes pericardial fluid into the pericardial sac, containing the heart, which in turn is a heterogeneous structure. In the model, the heart was simply modeled as a homogeneous volume with isotropic properties. This example illustrates the possibility for making an exceedingly complex numerical model, in order to maximize accuracy. Naturally, all numerical models must be based on simplifications. These can be based on estimations, theory and/or comparisons with physical experiments.

In the start of this project, estimates and results of previous studies indicated that a full three-dimensional study was feasible. However, it was found that a three-dimensional model introduced too much complexity for the scope of this project. The computational demands and intricacies were beyond the available time and resources, making it impractical to pursue. To balance accuracy and feasibility, the focus was turned to a simplified, lower-dimensional model. Simplifying the model ensures that the simulations are robust and executable, while still providing meaningful analysis. Despite these challenges, three-dimensional models are still assessed to be an important tool for the development of acoustic therapy. They provide detailed insights into the effect on targeted regions, ensuring effective treatments and avoiding injuries from misguided acoustic waves. Future work can gradually incorporate more complexity, eventually achieving representative three-dimensional simulations.

5.2 Verification strategy

To verify and improve the accuracy of the model, experimental work is crucial. Tissue phantoms mimic the acoustic and mechanical properties of biological tissues, providing a controlled environment for experiments. These measurements help verify the accuracy of simulation predictions and enable adjustments to the model for improved precision. Utilizing tissue phantoms bridges the gap between theoretical models and real-world applications in an ethical and economical manner. A needle hydrophone is an economical instrument, where some models allow for detailed pressure measurements within the tissue. This device can be used to capture high-resolution pressure data at specific points, facilitating a thorough comparison with the simulated pressure profiles. A laser doppler vibrometer can track particle velocity superficially, but is not suited for internal measurements.

In vivo or ex vivo trials, where acoustic wave profiles are mapped spatially in biological tissue, provide the next step for evaluating simulation results. Such studies can verify the accuracy of the model, in the complex environment that is biological tissue. Porcine models, i.e. pigs, have been employed in previous studies on CSWT [28].

5.3 Recommendations for further research

Given the limitations encountered in this project, several recommendations on future research can be made. As indicated above, experimental verification and tuning of a simulation model is of utmost importance. The evaluation of computationally economical simulation techniques can be motivated, as to make relevant three-dimensional models more feasible. Software tools for efficient manipulation of the mesh are also crucial for this. Electrical modeling, either numerical or analytical, of the piezoelectric transducer and its driving circuit is worth investigating as a means of aligning the outputs of the model with experimental results.

The reason that simulations of focal steering were not implemented was that the required three-dimensional simulations required too much computational resources. Only a static mesh was achievable with the approach recommended by COMSOL representatives, i.e. using the *Acoustic–Structure Boundary*. Coupled models utilizing adaptive meshing and time-stepping should be implemented by using the *Pair Acoustic–Structure Boundary, Time Explicit* multiphysics coupling. This would allow for much larger domain sizes.

Preliminary findings on the simulated systems also prompt recommendations on their further development. The feasibility of focal steering should be investigated further. Literature and numerical results from Section 4.3 indicate that a planar transducer has a narrow beam angle, decreasing the transmission angle variability. The feasibility of generating shockwaves with piezoelectric transducer elements adjacent to the body is also worth investigating further, as preliminary combined

results from Sections 4.2 and 4.3 indicate that the propagation distance is too short for shock formation. However, it is noted that little research has been made on the efficacy of non-shockwave acoustic therapy as an alternative to CSWT.

Although more men than women suffer from IHD, and require treatment, it is motivated to also implement a female anatomy model in the development of CSWT. The breast may limit the acoustic window, or hinder proper aiming of the transducer, which potentially could lead to accidental targeting and subsequent damage of lung tissue. Anatomical models of overweight or obese people are also highly relevant, as those in this demographic run a higher risk of suffering from IHD.

6
Conclusion

This project was done as part of a research project concerning the use of piezoelectric transducers for the application of CSWT. With this background, models for simulating the dynamics and resonance characteristics of single piezoelectric transducer disks were produced. Further, methods were developed for modeling the dynamics of transducer units, with backing and coupling layers and their generated acoustic fields. It could be shown that the frequency response and the time-domain signal was influenced by these features. These methods were based on an axisymmetric geometry. A one-dimensional model was implemented, facilitating the modeling of propagating planar waves in homogeneous or layered media. Further, a method for simulating a spherically focused, high amplitude signal was also developed, however not modeling the piezoelectric dynamics. A full three-dimensional simulation domain of the human thoracic region was constructed and attempts were made to run simulations. However, no successful simulations were run. Rather, priority was given to the lower-dimensional models and simplified geometries, described above.

Experimental verification and tuning of the simulation was planned and designed. For this, the design and manufacturing of a piezoelectric transducer unit was researched and planned. Due to practicalities, no such measurements were performed, and the models were never verified. It was decided not to calibrate and align the model with unreliable experimental data.

Preliminary results from the simulations indicate that the prototype hardware is able to create acoustic pulses with rise times on the order of 100 ns, on the threshold to be classified as shockwaves. Further, the achieved acoustic pressure is observed linear with applied voltage, and that acoustic waves with pressures of 0.5 MPa can be achieved in the upper range of tolerable driving voltages. These fields can be combined in a focal spot, increasing the pressures with orders of magnitude. However, it seems that the short propagation distance between the skin surface and the myocardium is too short to allow for shock formation with short (1-10 ns) rise times. High amplitude conventional soundwaves with non-linear effects were observed in the simulation outputs. It is possible that such acoustic signals have biological effects similar to those of CSWT, although the research in this area remains limited.

Bibliography

[1] World Health Organization. *Global Health Estimates 2020: Deaths by Cause, Age, Sex, by Country and by Region, 2000-2019*. 2020. URL: https://www.who.int/data/gho/data/themes/mortality-and-global-health-estimates/ghe-leading-causes-of-death.

[2] Swedish National Board of Health and Welfare. *Statistik om dödsorsaker 2022*. 2023. URL: https://www.socialstyrelsen.se/statistik-och-data/statistik/alla-statistikamnen/dodsorsaker/.

[3] Statistics Sweden. *Medellivslängden i Sverige*. 2023. URL: https://www.scb.se/hitta-statistik/sverige-i-siffror/manniskorna-i-sverige/medellivslangd-i-sverige/.

[4] E. Andersson et al. "Kostnader för hjärt-kärlsjukdom i Sverige 2019". In: *IHE Rapport 2021:4* (2021). URL: https://ihe.se/rapport/kostnader-hjart-karlsjukdom/.

[5] H.-T. Yang et al. "Cardiac shock wave therapy for coronary heart disease: an updated meta-analysis". In: *Brazilian Journal of Cardiovascular Surgery* 35 (2020), pp. 741–756.

[6] G. Burneikaitė et al. "Cardiac shock-wave therapy in the treatment of coronary artery disease: systematic review and meta-analysis". In: *Cardiovascular Ultrasound* 15.1 (Apr. 2017), p. 11. ISSN: 1476-7120. DOI: 10.1186/s12947-017-0102-y. URL: https://doi.org/10.1186/s12947-017-0102-y.

[7] G. Caspari and R. Erbel. "Revascularization with extracorporeal shock wave therapy: first clinical results". In: *Circulation* 100.Suppl 18 (1999), p. 84.

[8] V. Auersperg and K. Trieb. "Extracorporeal shock wave therapy: an update". In: *EFORT Open Reviews* 5.10 (Oct. 2020), pp. 584–592. ISSN: 2058-5241. DOI: 10.1302/2058-5241.5.190067. URL: http://dx.doi.org/10.1302/2058-5241.5.190067.

[9] L. Pölzl et al. "Defining a therapeutic range for regeneration of ischemic myocardium via shock waves". In: *Scientific Reports* 11.1 (Jan. 2021). ISSN: 2045-2322. DOI: 10.1038/s41598-020-79776-z. URL: http://dx.doi.org/10.1038/s41598-020-79776-z.

[10] Q. Qiu et al. "Cardiac Shock Wave Therapy in Coronary Artery Disease: A Systematic Review and Meta-Analysis". In: *Frontiers in Cardiovascular Medicine* 9 (July 2022). ISSN: 2297-055X. DOI: 10.3389/fcvm.2022.932193. URL: http://dx.doi.org/10.3389/fcvm.2022.932193.

[11] M. Delius et al. “Biological effects of shock waves: Lung hemorrhage by shock waves in dogs—pressure dependence”. In: *Ultrasound in Medicine & Biology* 13.2 (Feb. 1987), pp. 61–67. ISSN: 0301-5629. DOI: 10.1016/0301-5629(87)90075-5. URL: http://dx.doi.org/10.1016/0301-5629(87)90075-5.

[12] J. A. McAteer and A. P. Evan. “The Acute and Long-Term Adverse Effects of Shock Wave Lithotripsy”. In: *Seminars in Nephrology* 28.2 (Mar. 2008), pp. 200–213. ISSN: 0270-9295. DOI: 10.1016/j.semnephrol.2008.01.003. URL: http://dx.doi.org/10.1016/j.semnephrol.2008.01.003.

[13] C.-J. Wang. “Extracorporeal shockwave therapy in musculoskeletal disorders”. In: *Journal of Orthopaedic Surgery and Research* 7.1 (2012), p. 11. ISSN: 1749-799X. DOI: 10.1186/1749-799x-7-11. URL: http://dx.doi.org/10.1186/1749-799x-7-11.

[14] A. Kyriakou. “Multi-physics computational modeling of focused ultrasound therapies”. PhD thesis. ETH Zurich, 2015. URL: https://www.research-collection.ethz.ch/handle/20.500.11850/155142.

[15] D. L. Miller et al. “Overview of Therapeutic Ultrasound Applications and Safety Considerations”. In: *Journal of Ultrasound in Medicine* 31.4 (Apr. 2012), pp. 623–634. ISSN: 0278-4297. DOI: 10.7863/jum.2012.31.4.623. URL: http://dx.doi.org/10.7863/jum.2012.31.4.623.

[16] C. Slezak et al. “Physical Considerations for In Vitro ESWT Research Design”. In: *International Journal of Molecular Sciences* 23.1 (Dec. 2021), p. 313. ISSN: 1422-0067. DOI: 10.3390/ijms23010313. URL: http://dx.doi.org/10.3390/ijms23010313.

[17] A. S. Tenforde et al. “Best practices for extracorporeal shockwave therapy in musculoskeletal medicine: Clinical application and training consideration”. In: *PM&R* 14.5 (Apr. 2022), pp. 611–619. ISSN: 1934-1563. DOI: 10.1002/pmrj.12790. URL: http://dx.doi.org/10.1002/pmrj.12790.

[18] G. N. Sankin et al. “A multi-spark electrohydraulic shock wave generator with adjustable pressure field distribution and beam steering capability”. In: *Frontiers in Urology* 3 (Mar. 2023). ISSN: 2673-9828. DOI: 10.3389/fruro.2023.1057723. URL: http://dx.doi.org/10.3389/fruro.2023.1057723.

[19] R. S. Dahiya and M. Valle. *Robotic Tactile Sensing*. Springer Netherlands, 2013. ISBN: 9789400705791. DOI: 10.1007/978-94-007-0579-1. URL: http://dx.doi.org/10.1007/978-94-007-0579-1.

[20] COMSOL Multiphysics. *COMSOL Official Documentation - Piezoelectric Material*. 2019. URL: https://doc.comsol.com/5.5/doc/com.comsol.help.sme/sme_ug_theory.06.34.html.

[21] G. Kossoff. “The Effects of Backing and Matching on the Performance of Piezoelectric Ceramic Transducers”. In: *IEEE Transactions on Sonics and Ultrasonics* 13.1 (1966), pp. 20–30. DOI: 10.1109/T-SU.1966.29370.

[22] V. Rathod. “A Review of Electric Impedance Matching Techniques for Piezoelectric Sensors, Actuators and Transducers”. In: *Electronics* 8 (Feb. 2019), p. 169. DOI: 10.3390/electronics8020169.

[23] COMSOL Multiphysics. *Acoustics Module User's Guide*. 2023. URL: https://doc.comsol.com/6.2/doc/com.comsol.help.aco/AcousticsModuleUsersGuide.pdf.

[24] M.-C. Gosselin et al. "Development of a new generation of high-resolution anatomical models for medical device evaluation: the Virtual Population 3.0". In: *Physics in Medicine and Biology* 59.18 (Aug. 2014), pp. 5287–5303. ISSN: 1361-6560. DOI: 10.1088/0031-9155/59/18/5287. URL: http://dx.doi.org/10.1088/0031-9155/59/18/5287.

[25] V. F. Humphrey. "Nonlinear propagation in ultrasonic fields: measurements, modelling and harmonic imaging". In: *Ultrasonics* 38.1 (2000), pp. 267–272. ISSN: 0041-624X. DOI: https://doi.org/10.1016/S0041-624X(99)00122-5. URL: https://www.sciencedirect.com/science/article/pii/S0041624X99001225.

[26] V. Meesala, M. R. Hajj, and S. Shahab. "Shock formation distance—A design parameter for high power acoustic energy transfer systems". In: *The Journal of the Acoustical Society of America* 148 (Oct. 2020), pp. 2560–2560. DOI: 10.1121/1.5147105.

[27] Piezo.com Division of Mide Technology. *Materials Technical Data (Typical Values)*. 2020. URL: https://info.piezo.com/hubfs/Data-Sheets/piezo-material-properties-data-sheet-20201112.pdf.

[28] J. Holfeld et al. "Epicardial shock-wave therapy improves ventricular function in a porcine model of ischaemic heart disease: Shock wave treatment of ischaemic myocardium". In: *Journal of Tissue Engineering and Regenerative Medicine* 10.12 (May 2014), pp. 1057–1064. ISSN: 1932-6254. DOI: 10.1002/term.1890. URL: http://dx.doi.org/10.1002/term.1890.

DEPARTMENT OF MECHANICS AND MARITIME SCIENCES
CHALMERS UNIVERSITY OF TECHNOLOGY
Gothenburg, Sweden 2024
www.chalmers.se

CHALMERS
UNIVERSITY OF TECHNOLOGY